Charge distribution of metallic single walled carbon nanotube–graphene junctions

2014 New J. Phys. 16 013019

(http://iopscience.iop.org/1367-2630/16/1/013019)

New Journal of Physics
The open access journal at the forefront of physics
Deutsche Physikalische Gesellschaft DPG | IOP Institute of Physics

Charge distribution of metallic single walled carbon nanotube–graphene junctions

P T Robert[1,2] **and R Danneau**[1,2,3]

[1] Institute of Nanotechnology, Karlsruhe Institute of Technology, D-76021 Karlsruhe, Germany
[2] Institute of Physics, Karlsruhe Institute of Technology, D-76049 Karlsruhe, Germany
E-mail: romain.danneau@kit.edu

Received 8 October 2013, revised 19 December 2013
Accepted for publication 23 December 2013
Published 15 January 2014

New Journal of Physics **16** (2014) 013019

doi:10.1088/1367-2630/16/1/013019

Abstract

We report numeric and analytic calculations of the electrostatic properties for armchair carbon nanotube–graphene junctions. Using a semi-empirical method we first demonstrate that the equilibrium distance between a carbon nanotube and a graphene sheet varies with respect to the diameter of the carbon nanotube. We find significantly reduced values compared to AB-stacked graphene sheets in graphite, while even smaller value is found for a fullerene C_{60} implying a dimensionality dependence of the equilibrium distance between graphene and the other sp^2 carbon allotropes. Then, we use conformal mapping and a charge–dipole model to study the charge distribution of the carbon nanotube–graphene junctions in various configurations. We observe that the charges are accumulated/depleted at and near the vicinity of the junctions and that capped carbon nanotubes induce a significantly smaller charge concentration at their ends than the open-end nanotubes. We demonstrate that the carbon nanotube influence on the graphene sheet is limited to only few atomic rows. Such an influence strongly depends on the distance between carbon nanotube and the graphene sheet and scales with the carbon nanotube radius, while the potential difference does not modify the length over which the charge concentration is disturbed by the presence of the tube. By studying the potential landscape of carbon nanotube–graphene junctions, our work could be used as a starting point to model the charge carrier injection in these unconventional systems.

[3] Author to whom any correspondence should be addressed.

1. Introduction

Due to its outstanding physical properties, graphene is seen as a very promising material for many applications ranging from high frequency electronics to energy storage [1–3]. Usually, electrical devices made upon graphene flakes or films rely on their crystalline quality, their physical environment as well as their interconnectivity with other material [4, 5]. Indeed, connecting graphene has become a key issue to improve the performances of graphene-based devices [6–8]. Conduction in graphene depends not only on the conducting channel of the device but also on the metal/graphene interfaces. Depositing metal on graphene introduces an additional contact resistance, that contributes to reduce the overall conductance of the device. The mismatch between the work functions at the metal/graphene interface leads to a charge transfer and consequently to the doping of the graphene under the contacts [9–12]. This process is partly governed by the fact that the metal can be either chemisorbed or physisorbed [9, 10]. Moreover, the doping has been reported to extend to a large distance in the graphene far from the interface region creating pn-junctions or charge inhomogeneities even at high carrier density [13–17]. In addition, it has been shown that graphene is extremely sensitive to strain which is reflected in many of its electrical and optical properties [18–23]. Consequently, measurements of the contact resistance in graphene field-effect devices have shown inconsistency and the experimental values range over two orders of magnitude [7, 24–39]. This evidence shows that not only is the choice of the connecting material crucial but also the experimental conditions for its deposition, which can hinder precise control of the device fabrication.

In the search for reducing the contact resistance in sp^2 carbon devices, recent works have shown that graphitic materials could be an alternative to connect carbon nanotube (CNT) and graphene [40–46]. While graphene nanoribbon arrays have already been experimentally designed [47], theoretical expectations indicate that these tunable systems show a strong stacking dependence of the conductance and that they could be utilized as spin filters [48–51]. Indeed, there is an increasing interest in building full sp^2-carbon circuits, in particular by designing electrical devices with various sp^2-carbon allotropes [41, 52–59]. While graphene could be used as a transparent electrode, CNT could be used to contact graphene [60]. Density functional theory (DFT) calculations have demonstrated that for armchair single-walled tubes, the work function is close to the undoped graphene one ($\sim$4.48 eV) [61]. On the experimental side, measurements performed using ultra-violet photoemission spectroscopy gave values for the work function of CNT close to the one measured for graphene [62, 63]. Using CNT to connect graphene could prevent a large charge transfer and therefore could ensure a better integration into the graphene-device. Moreover from a mechanical perspective, since CNT are light materials, the strain effects on graphene should be minimal compared to the ones induced by the metal deposition. Raman spectroscopy experiments show that strain effects for deposited metals which have a high lattice mismatch with graphene introduce significant defects (i.e. Au and Ag in [64]). Since mechanical strains induce a change in the graphene work function (increase up to 0.64 eV for a 10% isotropic strain [20]), charge transfer between the metal and the graphene sheet may occur modifying the potential landscape in the vicinity of the contact, leading to a decrease in the device performances. We note that theoretical studies of covalently bond CNT–graphene hybrid systems have been reported [66–69] with potential application in energy storage [70] or supercapacitor [71]. Additionally, CNT would provide the smallest possible charge carrier injector to a graphene sheet.

Electronic transport experiments on sp^2-carbon hybrid structures have already been reported in the literature. For example, high conductance and low contact resistance were observed in CNT–CNT junctions [65, 72–74]. If only recently theoretical work succeeded to model the transport across a CNT–graphene junction [75] the first experiments in this field were performed more than a decade ago: conducting atomic force microscopy on CNT–graphite (i.e. highly oriented pyrolitic graphite) junctions were investigated using conductive atomic force microscopy in [76]. Resistance of the junction showed a strong dependence on the CNT–graphite lattice angle which was explained by the periodic mismatch of the electron momentum between both structures. More recently, the growth of CNT directly on few-layer graphene demonstrated the crystallographic alignment of the two respective lattices [77]. Hybrid CNT–graphene junctions have also been fabricated and tend to sustain that metallic CNT make good contact for graphene [52, 60, 78–80]. A Raman spectroscopy study of single walled metallic CNT covered by single layer graphene demonstrated that it is possible to detect a charge transfer occurring at the CNT–graphene junction [81].

In this work, we report an electrostatic study of CNT–graphene junctions. We are able to quantify the magnitude and the extension of the charge transfer induced when holding the CNT and the graphene at different electric potentials. We use analytic electrostatic calculations and an atomistic model, labeled as charge–dipole model, that includes the Coulomb interaction to compute the net charge distribution for both structures. This last model is able to handle structures with large number of atoms allowing a more extended overview of the system on a larger scale. We demonstrate a significant charge accumulation/depletion (depending on the sign of the voltage applied to the structures) in the graphene for atoms close to the junction region. A few atomic rows away from the CNT, the charge per atoms tends rapidly toward the neutrality. We conclude that the influence of the CNT on the graphene from an electrostatic point of view is spatially very limited.

This paper is organized as follows. First, we determine the CNT–graphene junction binding properties, mainly focusing on the equilibrium distance in section 2. The results provide thus accurate inputs for the following electrostatic calculations. In section 3.1, we then present analytic calculations of the CNT–graphene junction slice using two conformal transformations enabling us to determine the electrostatic potential in every point of the two-dimensional space and we detail the charge density inferred from them. Section 3.2 describes the charge–dipole model allowing us a more accurate description of the unusual geometry of our system. The results drawn from this atomistic model are commented in the subsections of section 3.2. Finally in section 4, we compare the results from our two-dimensional analytic calculations with the three-dimensional (3D) charge–dipole model.

2. Determination of the equilibrium distance between a carbon nanotube (CNT) and a graphene sheet

Calculations of the equilibrium distance between two sp^2-carbon allotropes have been already performed in the past essentially determining the distance between two graphene sheets in graphite [82–84]. More recently, binding energies and equilibrium distance between CNT and graphene have been reported in the framework of using the CNT as an atomic force microscopy tip [85–87]. In this work, we have computed the equilibrium distance between a CNT and a graphene sheet using the semi-empirical PM6-D method implemented in the MOPAC2009 package [88, 89]. The method based on a reparameterized neglect of diatomic differential

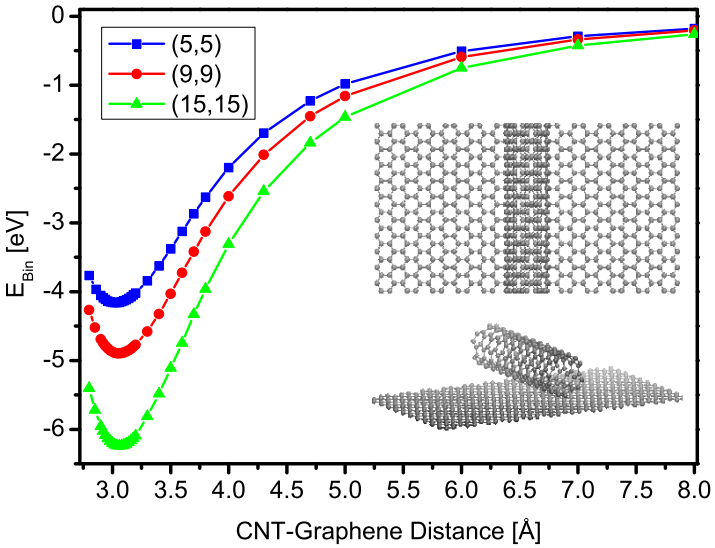

Figure 1. Binding energy for the CNT (5,5), (9,9) and (15,15) as function of the SWCNT–graphene distance. Inset: unit cell used for the calculation.

overlap method renders accurately the weak interaction that plays a fundamental role in sp^2 carbon hybrid structures. The weak interaction is the sum of two opposite contributions: the repulsive interaction due to the atomic orbital overlap and the attractive van der Waals forces. The van der Waals interaction handling has been improved for it by introducing a specific empirical term to account for the London dispersion energy as described in [90]. Recently, such a method has been used successfully to determine the bending of a suspended graphene sheet in a holey graphite structure [91].

In order to determine the equilibrium distance, we have performed binding energy calculations between several types of armchair CNT and a graphene sheet. We have calculated the total energy for different CNT–graphene distances $E_{\mathrm{Gra+CNT}}(d)$, as well as for the uncoupled system $E_{\mathrm{Gra+CNT}}(\infty)$. The binding energy $E_{\mathrm{Bin}}(d)$ for a distance between the CNT and the graphene set to d, is given by

$$E_{\mathrm{Bin}}(d) = E_{\mathrm{Gra+CNT}}(d) - E_{\mathrm{Gra+CNT}}(\infty).$$

The equilibrium distance is the distance for which the binding energy reaches its minimum.

For the calculations, a large unit cell ranging from 500 to 1500 atoms has been translated in order to reproduce the whole structure. The large length of the unit cell ($\sim$50 Å) leads to negligible intercell CNT–CNT interactions. A picture of the unit cell used for the calculations for a (5,5) single walled carbon nanotube (SWCNT) is represented in the inset in figure 1. In order to ensure the good convergence of our calculations, both structures are allowed to relax separately. All atoms of the graphene are free to relax in the in-plan directions. For the CNT, only the closest row of atoms to the graphene sheet is fixed, thus defining the distance CNT–graphene. The rest of the atoms is allowed to relax freely. The optimized geometry has been used for the self consistent field calculations.

The results for the binding energy calculations for a CNT (5,5), (9,9) and (15,15) are represented in figure 1. We observe that the equilibrium distance ranges from 3.02 Å for (5,5) to 3.06 Å for (15,15). It is clear that the equilibrium distance increases with the diameter of

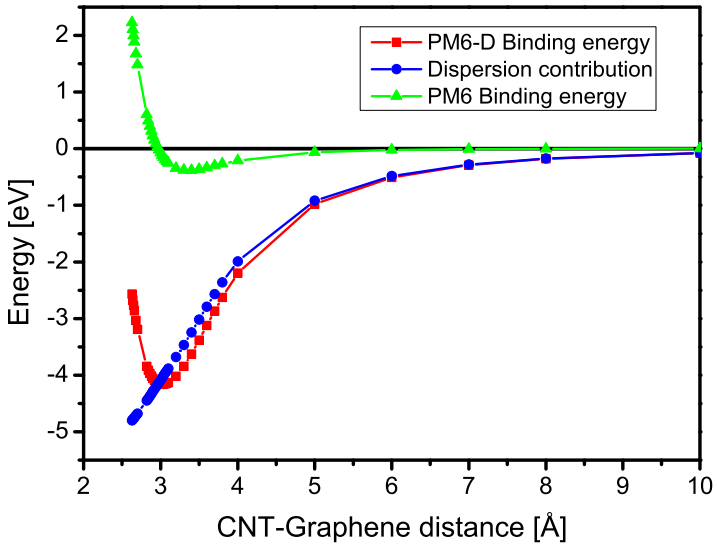

Figure 2. Binding energy obtained by the PM6-D method for the CNT (5,5) as function of the SWCNT–graphene distance. The London dispersion contribution as well as the binding energy obtained without considering the dispersion contribution (PM6 method) are also represented.

the tube (from 6.8 to 20.2 Å). Such a trend is in good agreement with previous studies [85–87] based on local-orbital DFT combined with intermolecular perturbation theory to render the van der Waals interaction as presented in [92, 93], while the values we obtained for the equilibrium distance are slightly higher. We believe that the difference in the obtained results could be due to the treatment of the repulsive interaction by both methods as well as to the amount of atoms that the calculations can handle.

The value of the equilibrium distance is far less than the inter-layer distance in multilayer graphene (∼3.4 Å experimental value). Differently from the multilayer graphene case, where all atoms are binding atoms, in the case of CNT–graphene systems, because of the CNT curvature, the only atoms restricted to a region close enough to both structures feel the repulsion due to the orbital overlap. The short-ranged repulsive energy contribution is thus more affected by the curvature than the long-ranged attractive van der Waals contribution, leading to a lowering of the equilibrium distance.

As previously mentioned, the specific London dispersion term in the PM6-D method is crucial to render properly the binding between graphitic structures. The lack of dispersion term as seen in figure 2 leads to a weaker binding (−0.38 eV compared to −4.16 eV for the PM6-D method) and as well as to a higher equilibrium distance, close to the interlayer distance in graphite. We confirm this trend by additionally performing similar calculations for a C_{60} molecule on a graphene sheet (see figure 3). We observe that the equilibrium distance is very much smaller than a (5,5) CNT which has the same diameter suggesting a dimensionality dependence of the equilibrium distance between graphene and the other sp^2 carbon materials.

We have used the calculated equilibrium distance (and the extrapolated values for very large diameter CNT, see appendix A) for our study of the charge distribution described in the following sections.

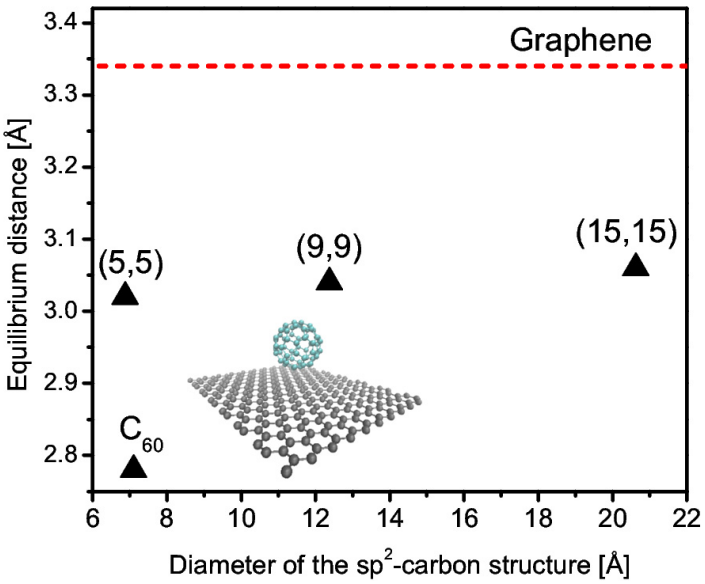

Figure 3. Equilibrium distance for a C_{60} molecule, a (5,5), a (9,9) and (15,15) CNT. The red dashed line represents the distance between two graphene sheet in a AB stacked configuration.

3. Charge distribution

3.1. Analytic modeling using conformal mapping transformations

Analytic electrostatic models have been used to exactly describe the charge distribution in CNT [94] and graphene [95]-based devices. In this section, we report exact two-dimensional solutions of the charge distribution in CNT–graphene junctions where the system is sliced perpendicularly to the CNT (see figure 4) using conformal transformation to solve exactly the Laplace's equation. This calculation technique [96] has already been applied successfully in graphene-based systems to obtain the transmission eigenvalues for a rectangular geometry [97]. We first calculate the charge distribution for a CNT–graphene junction using a two-dimensional classical electrostatic model while the junction is reduced into a circle and an infinite line representing the CNT and the graphene sheet, respectively. The Laplace's equation is solved for the considered geometry using two successive conformal mapping transformations. From the electrostatic potential, the linear charge density on the graphene sheet could be then inferred. We show that a strong charge accumulation occurs in the vicinity of the CNT–graphene interface. However, the amount of charges decreases sharply with the distance to the junction. We also characterized the length over which the CNT has a significant influence on the charge distribution in the graphene sheet. Note that for simplification we still denominate the CNT by their chiral number (n,m) while they are just distinguished by their corresponding radii.

3.1.1. Laplace's equation. Here we assume that for very large graphene sheets, edge effects can be neglected. If we consider the graphene–CNT junction far from the edges, the graphene can be modeled by an infinite straight line parallel to the x-axis. The CNT is approximated by a circle of radius $R_{\mathrm{cnt},0}$ and is placed at a distance $R_{\mathrm{cnt},0}+\epsilon$ above the graphene. We use for ϵ the values calculated from section 2. We consider that the potential difference between the CNT

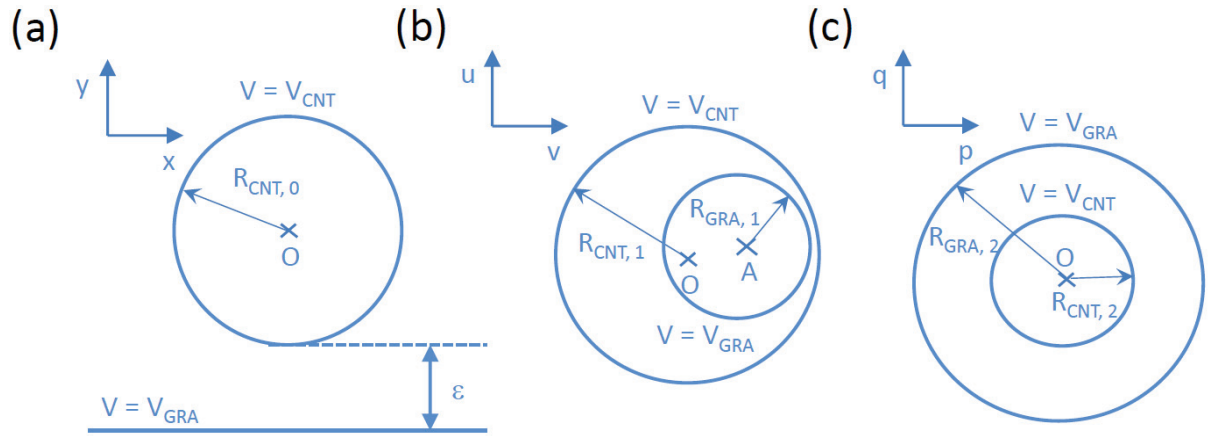

Figure 4. (a) Initial geometry of the sliced CNT–graphene junction where the CNT is represented by a circle placed at a distance υ form a graphene flake represented by an infinite line. (b) Geometry obtained by transforming the initial geometry via the first conformal transformation. (c) Final geometry obtained via the second conformal mapping.

and the graphene sheet does not reduce ϵ (which corresponds to the equilibrium distance of the previous section), since the strong repulsive forces should counteract the electrostatic attraction. A diagram of the initial geometry is drawn in figure 4(a). The graphene and the CNT are set to a potential V_{gra} and V_{cnt}, respectively. These boundary conditions and the Laplace's equation

$$\nabla^2 V = 0 \tag{1}$$

determine the electrostatic potential V for the above described geometry.

This particular Dirichlet problem cannot be solved straightforward. Since the Laplace's equation is known to be invariant under conformal transformation, we successively applied two conformal maps in order to transform the initial geometry into a solvable problem (see appendix B for calculation details). The first transformation maps the initial circle and the initial line into two non-concentric circles. The second one maps the non-concentric circles into concentric circles (see figure 4).

3.1.2. Charge density. The final geometry (figure 4(c)) matches the one of a capacitor made of two infinitely long concentric cylindrical shells. The inner cylinder (radius: $R_{\mathrm{cnt},2}$) is set at a potential V_{cnt} while the outer cylinder (radius: $R_{\mathrm{gra},2}$) is set at V_{gra}. In this configuration the Laplace's equation can easily be solved. The potential between the two cylinder capacitor is then given by

$$V(p,q) = V_{\mathrm{cnt}} + \frac{\Delta V}{c}\left(\ln\left(\sqrt{(p^2+q^2)}\right) - \ln\left(R_{\mathrm{cnt},2}\right)\right), \tag{2}$$

where $\Delta V = V_{\mathrm{gra}} - V_{\mathrm{cnt}}$ and $c = \ln(\frac{R_{\mathrm{gra},2}}{R_{\mathrm{cnt},2}})$.

Using the expression of $p(x, y)$ and $q(x, y)$ in equation (2) yields the potential for the initial geometry $V(x, y)$. A map of the electric potential is represented in figure 5 for a CNT (5,5) with $V_{\mathrm{cnt}} = 10\,\mathrm{V}$ and $V_{\mathrm{gra}} = 1\,\mathrm{V}$. As expected, the potential drop at the junction region occurs at the smallest area developing the strongest electric field. Since our sliced junction is a

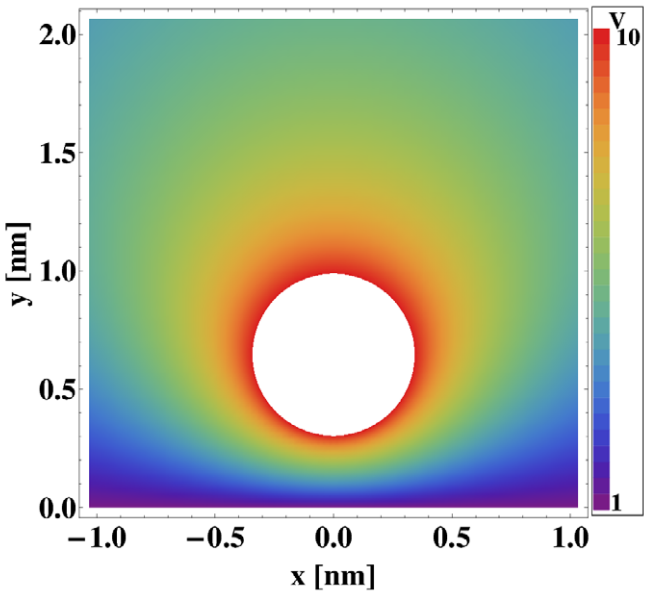

Figure 5. Color map of the electrical potential for a CNT (5,5). The tube is shown as a white circle. The potential of the nanotube is $V_{\mathrm{cnt}} = 10\,\mathrm{V}$ whereas the graphene is maintained at the potential $V_{\mathrm{gra}} = 1\,\mathrm{V}$.

two-dimensional system, the linear charge density $\lambda(x)$ for the graphene sheet is given in the $(O_{x,y}, x, y)$ coordinate system by

$$\frac{\partial V}{\partial x}(x, y) = -\frac{\lambda(x)}{\epsilon_0}. \tag{3}$$

Figure 6 shows $\lambda(x)$ for CNT (5,5), (9,9), (20,20) and (37,37) with $V_{\mathrm{cnt}} = 10\,\mathrm{V}$ and $V_{\mathrm{gra}} = 1\,\mathrm{V}$.

The charge density profile exhibits a sharp peak in the junction region. The charge accumulation does occur in a region in the vicinity of the CNT–graphene junction, as the charge density profile tends quickly toward neutrality away from the junction. The influence of the CNT on the charge distribution in the graphene sheet is thus spatially limited to a small portion of it. The maximum charge accumulation is around $-1.45e\,\mathrm{nm}^{-1}$ for the CNT (5,5) while for larger radius CNT the maximum is around $-1.55e\,\mathrm{nm}^{-1}$. This means that the radius of the CNT plays a less significant role on the maximum of charge accumulated as the distance between the CNT and the graphene sheet. The effect of the radius on the overall shape of the charge density is also limited. Only the width of the peak in the charge density profiles of CNT with smaller radius is broader than ones for CNT with large radius. Thus, when normalized to their radius, CNT with smaller radius tends to have a deeper influence on the graphene sheet charge distribution than CNT with larger radius (as we saw in the previous sections, the smaller the CNT radius the closer to the graphene sheet).

Despite the fact that these analytic calculations produce exact solutions, the CNT and the graphene sheet geometries are dramatically simplified. The atom positions are not taken into account and it is not possible to visualize the charges at the apex of the tube. In the following section, we use a numerical method which allows to accurately account for the geometry of the junction.

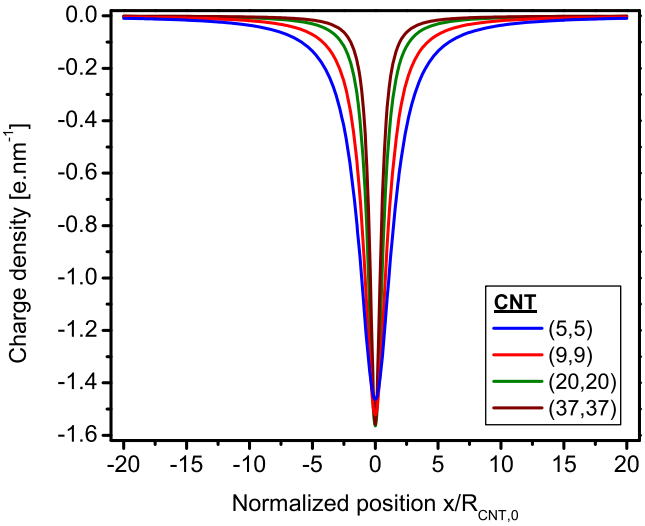

Figure 6. Charge density for the CNT (5,5), (9,9), (20,20) and (37,37) with $V_{\mathrm{cnt}} = 10\,\mathrm{V}$ and $V_{\mathrm{gra}} = 1\,\mathrm{V}$. The distances have been normalized to the radii of the tubes. This representation shows that ϵ has a stronger influence than the radius of the CNT on the charge distribution on the graphene sheet in the proximity of the junction.

3.2. Numerical calculations using the charge–dipole model

3.2.1. Presentation of the charge–dipole model. Using analytic calculations, we have seen that the influence of the CNT on the graphene charge distribution is restrained to regions of a few nanometers. In this section we have used a 'charge–dipole' 3D model to study the CNT–graphene junctions down to the atomic scale. The charge–dipole model associates to each atom i, a net charge q_i and a dipole $\mathbf{p}_i$. The electronic configuration of the sp^2-carbon structure is then well reflected: the net charge accounts for the π-electrons and the dipole accounts for the σ-electrons. For a given spatial distribution of atoms, the total electrostatic energy E_{tot} is minimized in order to compute the $\{q_i, \mathbf{p}_i\}$ associated with each atom.

The model has been first suggested by Orlon [98] in an extension to previous works on the polarizations of molecules. The idea of associating to each atom of a molecule a net charge and a dipole to compute electronic properties of molecules structures has then been used successfully by Appliquing *et al* [99] and Stern *et al* [100]. The first sp^2 carbon allotrope system was studied by Shanker *et al* [101] in the framework of the polarizability of C_{60} molecules. It has been presented in its current development by Mayer in 2005 who found a satisfying renormalization of the model to avoid the divergence arising when a point distribution of charge is considered [102, 103]. Additionally, the charge–dipole model was successfully used in modeling the electric field induced deformations of CNT cantilevers [104] and the charge rearrangement in charged CNT [105].

In a recent work, this model was successfully used to compute the charge distribution in a relaxed graphene sheet [106]. The results were compared to a classical electrostatic analytic model. The model was able to give a satisfying description of the charge enhancement effects on the edge of the graphene.

In this section, we describe the charge–dipole model as it has been presented and parameterized by Mayer in 2005 and extended in 2007 [103, 107]. The total electrostatic energy

for a N atoms configuration and its associated charge–dipole values $\{q_i, \mathbf{p}_i\}$ is given by

$$E_{\text{tot}} = \frac{1}{2}\sum_{i\neq j} q_i T^{i,j}_{q-q} q_j - \sum_{i\neq j} q_i \boldsymbol{T}^{i,j}_{q-p}\mathbf{p}_j - \frac{1}{2}\sum_{i\neq j}\mathbf{p}_i \boldsymbol{T}^{i,j}_{p-p}\mathbf{p}_j + \frac{1}{2}\sum_{i=1}^{N} q_i T^{i,i}_{q-q} q_i - \sum_{i=1}^{N} q_i \boldsymbol{T}^{i,i}_{q-p}\mathbf{p}_i$$
$$-\frac{1}{2}\sum_{i=1}^{N}\mathbf{p}_i \boldsymbol{T}^{i,i}_{p-p}\mathbf{p}_i + \sum_i q_i(\chi_i + V_{i,\text{ext}}) - \sum_i \mathbf{p}_i \cdot \mathbf{E}_{i,\text{ext}}. \tag{4}$$

For an atom i, χ_i is the affinity of the atom i, the external potential is $V_{i,\text{ext}}$ and external electrostatic field is $\mathbf{E}_{i,\text{ext}}$. The three first terms in E_{tot} are the mutual interaction terms between atoms, the next three terms contain the self-energy terms whereas the two last terms are the single atom interaction terms. The terms T_{q-q}, $\boldsymbol{T}_{q-p}$, $\boldsymbol{T}_{p-p}$ contain, respectively, the charge–charge, charge–dipole, dipole–dipole interactions in vacuum.

In order to be able to define the terms $T^{i,i}_{q-q}$, $\boldsymbol{T}^{i,i}_{q-p}$, $\boldsymbol{T}^{i,i}_{p-p}$, which diverge for a point charge distribution when $r_{i,j} \to 0$, the charge density for each atom has been regularized by a Gaussian distribution centered on the atom. The atom i bearing a charge q_i has its charge distribution given by

$$\rho_i(\mathbf{r}) = \frac{q_i}{\pi^{3/2}R^3}\exp\left(-\frac{|\mathbf{r}-\mathbf{r}_i|^2}{R^2}\right), \tag{5}$$

where R is the width of the Gaussian distribution.

The parameter R has been set in the calculation to 0.068 62 nm, as used in previous works [102, 103, 106–110]. This value corresponds for carbon sp^2 structures, to a polarizability of $\frac{\alpha_{\text{iso}}}{4\pi\epsilon_0} = 0.121\,490\,01$ nm.

For a system of N atoms, the $\{q_i, \mathbf{p}_i\}$ for each atom are determined by minimizing the total electrostatic energy E_{tot} given by equation (4). The minimization is carried by requiring that for each atom i

$$\frac{\partial E_{\text{tot}}}{\partial q_i} = 0 \quad \text{and} \quad \frac{\partial E_{\text{tot}}}{\partial \mathbf{p}_i} = 0$$

leading to solve a $4 \times N$ linear equation system.

If the sum of the net charge is required to be equal to a specific value Q_{tot}, an additional equation has to be solved. The minimization of the expression $E_{\text{tot}} - \lambda(\sum_i q - Q_{\text{tot}})$ with respect to the variable λ leads to the additional equation.

3.2.2. Geometry. The CNT–graphene junction has been modeled by a rectangular flake of graphene and a CNT placed on top of the graphene flake. The length of the in-plane bound between two carbon atoms has been set to 0.142 nm. We used the distance ϵ between the graphene and the CNT determined by the PM6-D semi-empirical quantum chemical method presented in section 2. For a CNT (5,5), ϵ is taken as 3.02 Å through all calculations unless it is specified. The coordinate system used for the calculation is represented in figure 7. The stacking of the atoms is A–B, meaning that for the CNT, its closest atoms to the graphene flake on the center of an hexagonal cell.

For the graphene sheet, we have fixed the width of the sheet all through the calculations to $w \sim 5.00$ nm and we have taken several lengths for the sheet ranging from $l \sim 5.00$–50.00 nm, which corresponds to a number of atoms from $N_{\text{gra}} = 984$–9512. Although the charge–dipole

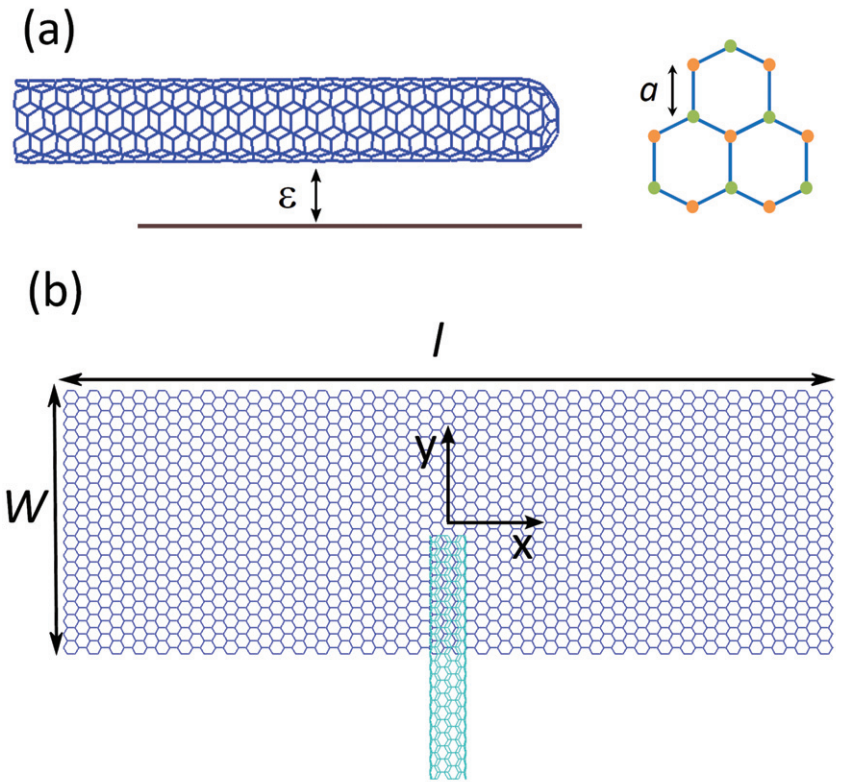

Figure 7. Geometry of the studied CNT–graphene junctions: Parameters and coordinate system used for our calculations.

model does not take into account the band structure of the CNT and the graphene sheet, for the coherence of our study we have taken armchair CNT to form the junction. For most of the calculation we have chosen a (5,5) CNT that has been made by repeating 19 elementary cells in the y direction, thus having a non-caped length of about 4.60 nm and containing $N_{\mathrm{cnt}} = 380$ atoms. The junction length (i.e. the length of the part of the CNT lying on top of the graphene sheet) is $\sim$2.25 nm, the rest of the CNT lays suspended outside the flake in straight manner. For capping the CNT, we use a C_{30} hemisphere made by halving of a C_{60} molecule ($N_{\mathrm{cnt}} = 420$). The free standing end was left uncapped.

3.2.3. Code validation. In this part, we validate our code by reproducing results already published on graphene and CNT prior to study the CNT–graphene junction. We demonstrate that the charge–dipole model is poorly sensitive to changes induced by the geometry relaxation processes and only on the very edge of the system. The charge–dipole model reveals smoother charge distribution and no variation in the bulk of the system.

Charge accumulation effect at the edges of a graphene sheet has already been calculated numerically [111, 112] and also by using analytic electrostatic model [95]. Wang and Scharstein [106] confirmed this result for a rectangular graphene sheet held at a potential V_0 with a certain amount of external charges using a charge–dipole model. The net electric charge tends to accumulate on the edges and on the corners. The authors used a charge–dipole based model to compute the charge distribution on free-standing relaxed graphene. The graphene sheet was relaxed by using adaptive inter-molecular reactive bond order potential functions.

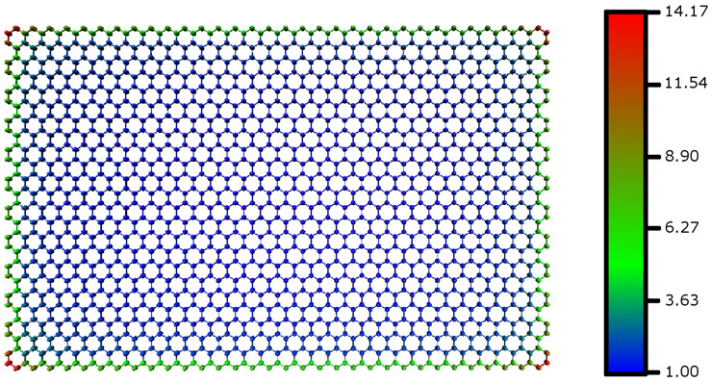

Figure 8. Density of net charge for a rectangular graphene sheet. A color scale has been used to represent the charge density for each atoms. Red stands for a high charge density, blue for a lower one. The density has been normalized to the one in the middle of the graphene flake: $q_0 = 8.1 \times 10^{-4}\, e$ per atom.

We carried out the same calculations by without any relaxation of the geometry and compared our results to the one obtained in [106].

A rectangular graphene sheet (dimensions: $x = 8$ and $y = 5$ nm) has been used for the calculations generated with the parameters described in section 3.2.2. Here, the graphene flake was held at a potential of $V_{\mathrm{gra}} = 1$ V.

Figure 8 reproduces the results for the unrelaxed graphene sheet. The edges and corners charge enhancement effects are clearly observed. The range of the normalized charge density is consistent with the results by Wang [106], reaching its maximum value at the corners (i.e. about 14 times the density at the center of the flake). We see here that the results obtained in a non-relaxed structure is very similar to the relaxed one.

We have also performed calculations in an uncapped (5,5) CNT. The structure was not relaxed. We imposed the CNT to have a total charge $Q = 20e$. The results are compared to those obtained using different calculation methods [113–115] (see figure 9). The expected U-shape curve for the density was obtained. Again, our calculations for an unrelaxed structure is fairly similar to the relaxed one. The value of the density differs slightly for the atoms at the edge of the CNT. DFT and moment method results depart more from the results obtained for both unrelaxed/relaxed structures with the charge–dipole model. This is particularly true for the end atoms since the normalized charge density given by the charge–dipole is around 1.8–2 whereas for the DFT and moment method it is around 2.5–2.7. This qualitative agreement between all of these methods (excess of charges at the edge of the CNT), the change of the charge density is smoother for the charge–dipole model. We also note that the DFT calculations produce an unexpected variation at the center of the CNT which is somewhat difficult to interpret.

Here we have demonstrated that our program is able to reproduce the already existing results and we show that the effect of relaxation is very limited. In the following sections we apply our code to the CNT–graphene junction for various configurations.

3.2.4. Scaling and effect of the junction region on the graphene sheet. In this part, we study the effect of the CNT on graphene sheets with different sizes. This allows us to determine from which size of the system we can consider that the edge effect does not influence the charge distribution at the junction itself. When the graphene is held at a potential of $V_{\mathrm{gra}} = 1$ V while the

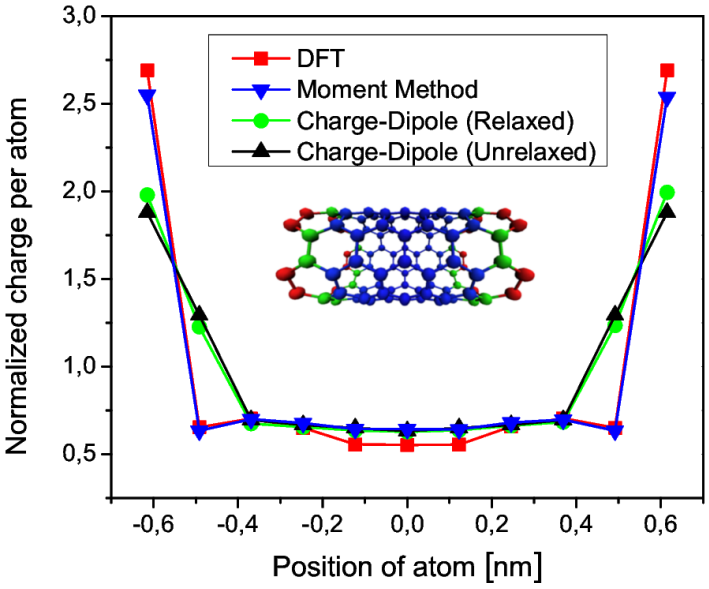

Figure 9. Normalized charge density along the (5,5) CNT axis with respect to the average net charge per atom. The results for the unrelaxed/relaxed CNT using the charge–dipole model are plotted, as well as results of the DFT calculations from [114] and results of moment method from [115]. Inset: net charge per atom. The blue color indicates a low net charge while the green denotes a significant amount of net charge and the red color denotes strong accumulation of charge.

CNT is set at $V_{\text{cnt}} = 10\,\text{V}$, the net charge per atom in the graphene flake experiences considerable variation close to the junction region. The closest the graphene atoms are located to the CNT, the stronger the effects on the charge profile are. In order to determine the length over which the graphene atoms feel the influence of the CNT, calculations with several lengths for the graphene flake have been performed. We study the net charge distribution in the graphene along the length of the sheet near the junction region as well as far from the CNT, following the line drawn in the inset of figure 10. The edge effects is then presented in section 3.2.6.

Figure 10(a) shows clearly that the charge profile does not change significantly around the junction region with the length of the graphene sheet. The charge depletion peak in the charge profile has the same shape through all calculations. For a length of about $l \sim 5.00\,\text{nm}$, the minimum is about $-10.97 \times 10^{-2}\,e$ per atom when for about $l \sim 50.00\,\text{nm}$ it is about $-10.85 \times 10^{-2} e$ per atom. These values correspond to the net charge carried by the closest atom to the CNT. The further the graphene atoms are from the CNT, the weaker is the charge depletion. For atoms located a few nm ($x \geqslant 2$–$3\,\text{nm}$) away from the CNT, the charge profile flattens when the influence of the CNT becomes less prevalent.

Narrower graphene sheets exhibit stronger edge effects which modify the charge distribution up to $-2.76 \times 10^{-2}\ e$ per atom for a $l \sim 5.00\,\text{nm}$ length. With increasing length, the edge effects become less significant. For lengths around 40 nm, the edge effects are almost irrelevant. One effect of the scaling is that for lengths larger than $\sim$15 nm, the net charge value reaches, for atoms located away from the CNT, almost a neutral value. Thus meaning that the influence of the CNT is restrained to a few atomic rows near the junction region. For smaller

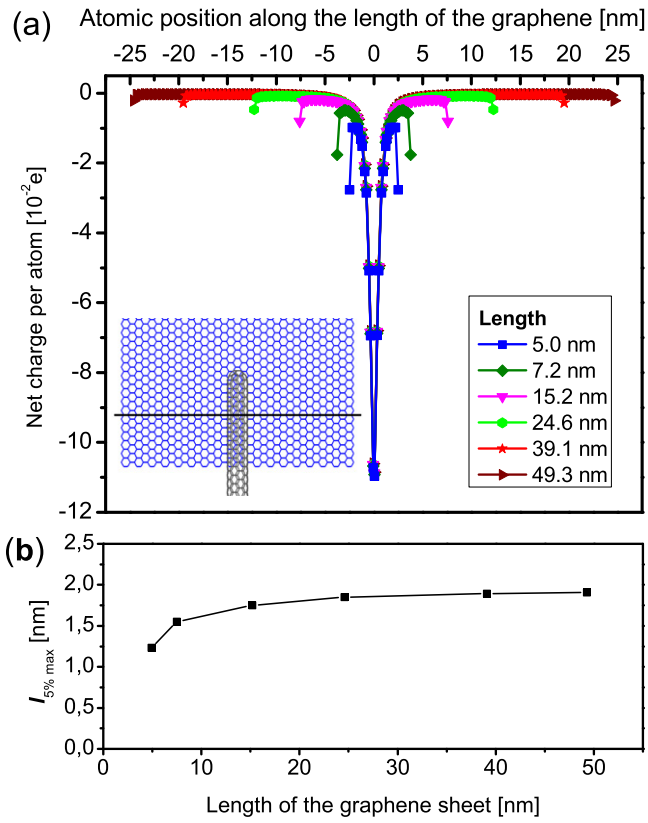

Figure 10. (a) Net charge per atom in the junction region along the width of the graphene sheet. Different widths for the graphene sheet have been used. (b) Length on the graphene sheet where the net charge corresponds to $|q|_{5\%\,\max}$ for different graphene sheet lengths.

sheets, the influence of the CNT is still strong near the edges of the graphene since the net charge value stays well above the neutrality.

The value $|q|_{5\%\,\max}$ corresponding to 5% of the maximal absolute value for the net charge is located in the part where the charge profile starts to flatten. Thus, the length on the graphene sheet $l_{5\%\,\max}$ where the net charge profile reaches $|q|_{5\%\,\max}$ is a good indicator of how far the CNT affects the charge distribution in the graphene sheet. In figure 10(b), $l_{5\%\,\max}$ has been represented for different values of graphene sheet lengths. The influence of the CNT increases with the length of the graphene. For small lengths it is limited to the very few atomic rows near the junction. $l_{5\%\,\max}$ reaches a value around 1.90 nm eventually and does not show significant changes with the scaling. Hence, this value can be taken as reference for the extent of the CNT influence on the graphene. Therefore, for our investigation we have chosen graphene sheets that are sufficiently large enough that $l_{5\%\,\max}$ is already saturated.

3.2.5. Charge distribution profile in the graphene sheet and the CNT. Here we study the charge distribution profile for both structures. We also investigate how the net charge distribution changes for an uncapped and a capped CNT. Using the conclusions of section 3.2.4 to determine a suitable geometry, we choose a graphene sheet with a length about $\sim$24.6 nm for our study.

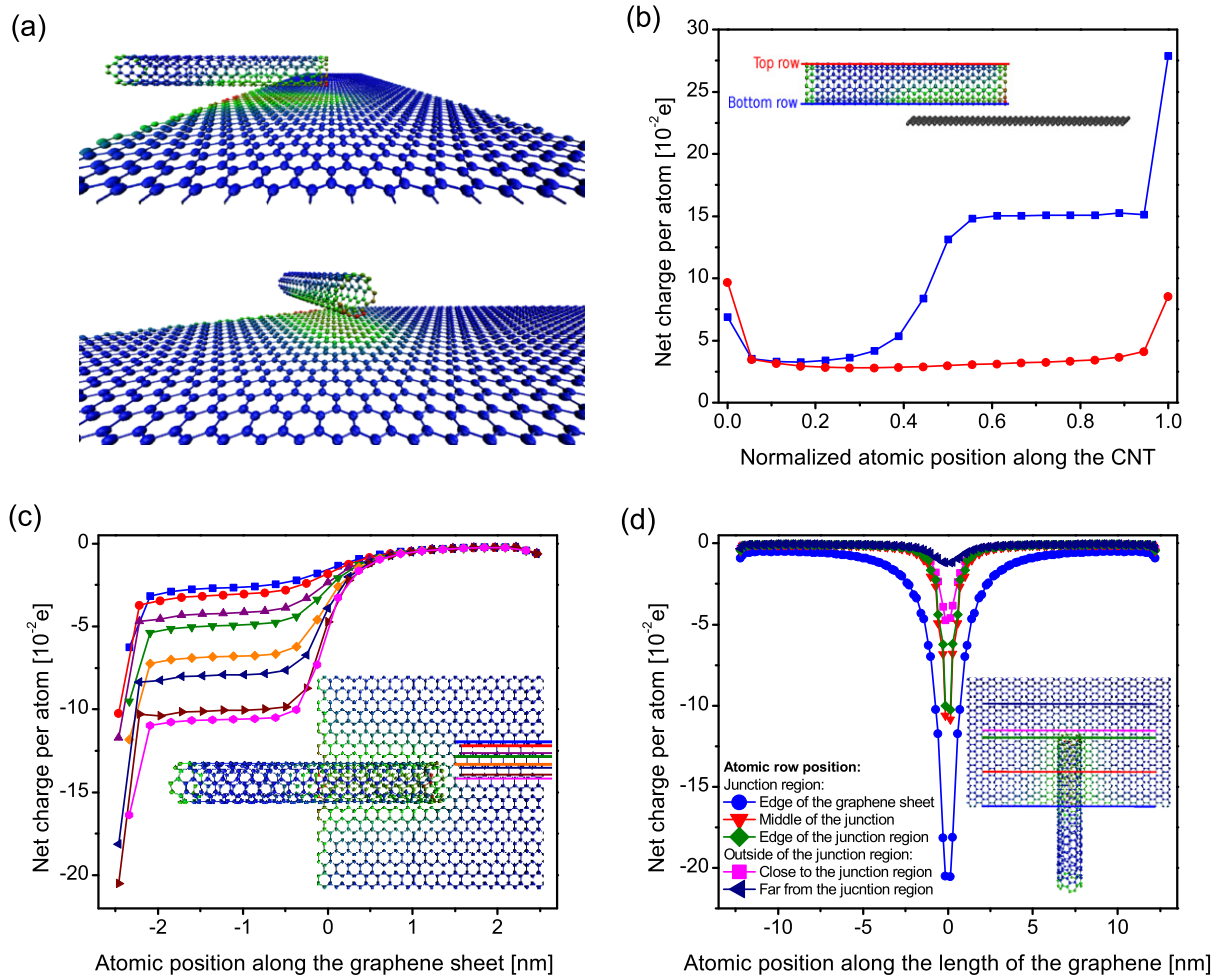

Figure 11. (a) Net atomic charge density for an uncapped metallic CNT (5,5)-graphene junction. The net charge has been normalized for the CNT as well as for the graphene to the average charge per atom for each structure. The blue color indicates a net charge close to the average while the green denotes a significant variation to the average and the red color denotes a strong variation to the average. (b) Net atomic charge density for an uncapped (5,5) metallic CNT part of a (5,5) CNT–graphene junction. The charge has been represented for the top atomic row and for the bottom atomic row. (c) Net charge density profile along the width of the graphene flake for different rows of atoms. The colors correspond to the different atomic rows with $x = \text{cst}$. (d) Net charge profile along the length of the graphene flake for different rows of atoms. The colors displayed in the top figure correspond to the different atomic rows with $y = \text{cst}$.

First we examine the junction uncapped (5,5) CNT–graphene. The average charge per atom has been computed for each structure as well as the net charge distribution. The average net charge per atom in an uncapped (5,5) metallic CNT–graphene junction was found to be $\overline{q}_{\text{cnt}} = \sum_{\text{cnt}} q_i / N_{\text{cnt}} = 5.71 \times 10^{-2} e$ per atom for the CNT and $\overline{q}_{\text{gra}} = \sum_{\text{gra}} q_i / N_{\text{gra}} = -0.46 \times 10^{-2} e$ per atom for the graphene.

From figure 11(a), it can be seen that the net charge value significantly differs from the average net charge for the atoms located close to the junction region. The strongest variations

are to be found at the extremity of the CNT that lays on top of the graphene and at the edge of the graphene sheet under the CNT.

It can be noticed (figure 11(b)), that the atoms on top of the CNT do not experience a significant change in their net charge until the very few extremity atom rows. The net charge ranges from 2.80 to $3.57 \times 10^{-2}e$ per atom for these atoms but the two end atoms, which have much higher charge due to the edge effects. Such an observation contrasts with the bottom atoms of the CNT which feel the strong influence of the graphene flake. These atoms see their net charge increase on the junction part, their net charge ranges then from 1.30 to $1.56 \times 10^{-1}e$ per atom for the end atom, which has the highest net charge value and feels the highest edge effects. Besides on the junction part, except for the end atom, the net charge distribution does not experience a strong variation.

On the graphene flake, this behavior can also be observed. Aside from the edge atoms, figure 11(c) shows that for the junction part the net charge profile does not change significantly along the length of the junction. Still, the profile changes with the distance to the axis of the CNT. For the atoms outside the junction region, the charge profile tends quickly toward the neutrality.

For the row of atoms placed at a distance $x = 0.071$ nm of the tube axis (i.e: the closest atoms to the CNT axis), the net charge per atom varies from -10.02 to $-10.96 \times 10^{-2}e$ per atom excluding the edge atom (the pink curve in figure 11(c)). While for the row placed at $x = 0.355$ nm away from the tube axis, which is a value close to the radius of the (5,5) CNT, the net charge ranges from -6.2 to $-7.3 \times 10^{-2}e$ per atom (the orange diamonds in figure 11(c)).

Further away from the CNT axis, the effects of the CNT combined with the charge enhancement effects on the edges lead to a more pronounced decrease of the net charge value along the length of the junction with y increasing. Even so, for a row placed at $x = 0.781$ nm away from the CNT axis, the net charge per in the junction region remains around $-3.1 \times 10^{-2}e$ per atom.

As seen in figure 11(d), the charge profile along the length of the graphene flake for atomics rows with negative y show no major difference, edge row of the graphene sheet set apart. The charge profile shows a dramatic variation for atoms close to the CNT, while it decreases steeply a few atomic rows away from the CNT axis ($l_{5\%\,\mathrm{max}} \sim 1.9$ nm) and thus reaches a plateau value that is close to the electrical neutrality.

The ideal open-end CNT have non-terminated sharp edges, leading to a strong charge accumulation at the end of the CNT. However, capped CNT that can be terminated by a half-fullerene structure. The absence of non-terminated atoms at the end of the CNT is expected to show less edge effects, i.e. a reduced charge accumulation at the end of the junction. Moreover, from an experimental point of view, CNT are known to be either capped or uncapped [116]. The nature of the ends cannot be predicted and are potentially hard to control. We compute the average net charge for both structures this time using a capped CNT (5,5). The values of the average net charges lie in the same range as in the calculation made with an uncapped CNT: for the CNT $\overline{q}_{\mathrm{cnt}} = \sum_{\mathrm{cnt}} q_i / N_{\mathrm{cnt}} = 5.62 \times 10^{-2}e$ per atom and for the graphene $\overline{q}_{\mathrm{gra}} = \sum_{\mathrm{gra}} q_i / N_{\mathrm{gra}} = -0.50 \times 10^{-2}e$ per atom.

For the CNT, capped end set apart, figure 12(a) shows that capping the end of the CNT does not affect the charge profile along the length of the tube. The charge profile along the tube shows a similar behavior as in figure 11(b). The results of the calculations clearly demonstrate that the edge effects are much less prevalent at the junction end of the capped nanotube than on the case of an uncapped CNT. The atom with the maximal net charge in the CNT is still to be

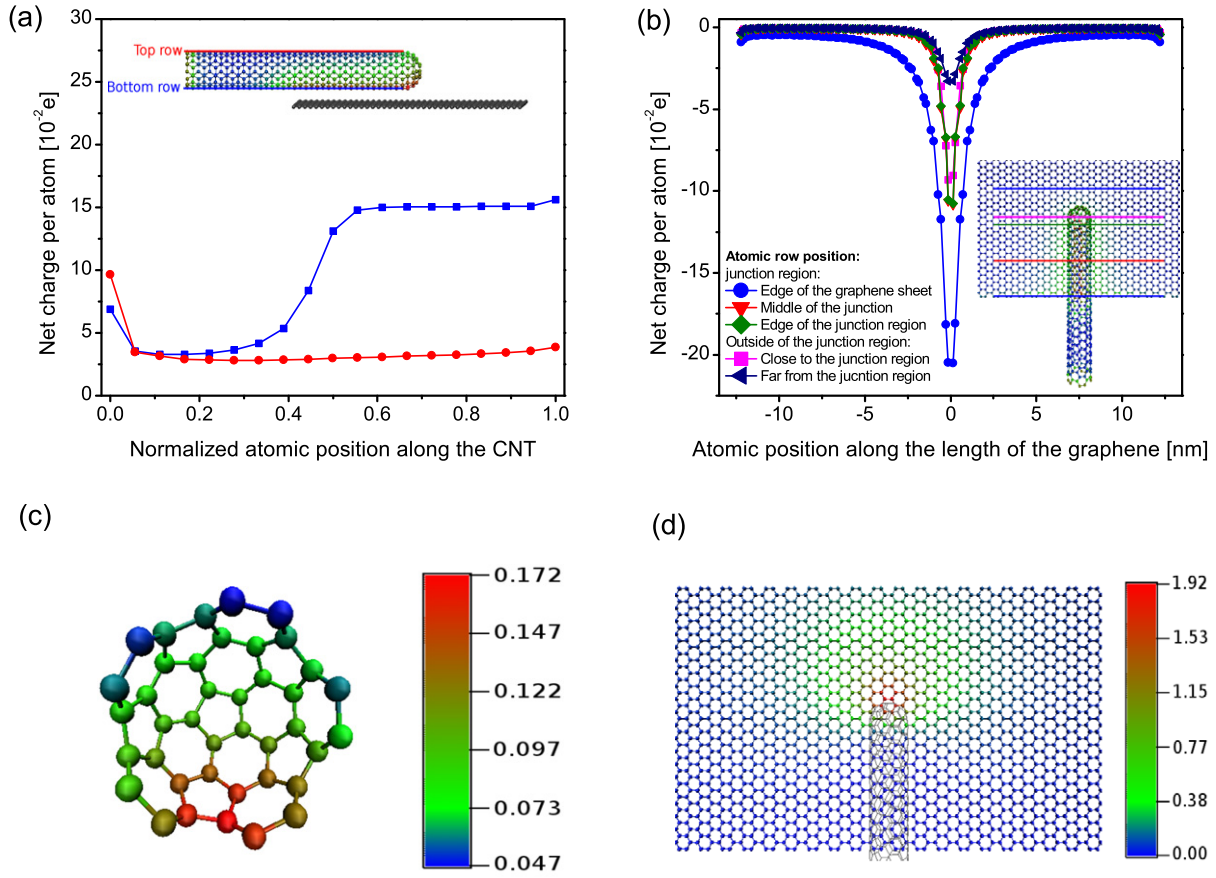

Figure 12. (a) Net atomic charge density for a capped(5,5) metallic CNT part of a (5,5) CNT–graphene junction. The charge has been represented for the top atomic row and for the bottom atomic row. (b) Net charge per atom along the length of the graphene flake for different atomic rows. The (5,5) CNT has been capped with a C_{60} molecule at one end. (c) Net charge for the atoms belonging to the cap of the (5,5) CNT. The color scale indicates the value of the net charge in e. (d) Relative difference in the charge density in the junction region part of the graphene sheet when considering a capped nanotube over an uncapped nanotube. The relative difference is given by $(q_{\mathrm{gra,capped}} - q_{\mathrm{gra}})/q_{\mathrm{gra}}$. The color scale gives the percentage of difference.

found at the junction end, but with a significant lower charge density than before. Indeed, for a uncapped CNT, the maximal net charge was $2.79 \times 10^{-1}e$ per atom when for a capped nanotube its value is $1.72 \times 10^{-1}e$ per atom as can be observed in figure 12(c).

Concerning the graphene flake, the overall charge profile shape does not show significant difference with the non-capped case (see figure 12(d)). The induced changes on the charge profile when using a capped CNT are shown in figure 12(d). As expected these changes are concentrated near the cap region, thus the atoms close to the cap experience the most significant variations in their net charge. For the closest atoms to the cap, the increase in the net charge is about 1.92 times the value of the charge density in the uncapped CNT. These changes are reflected in the average carried net charge of the graphene flake $\overline{q}_{\mathrm{gra,\,capped}}$ which is higher than in the uncapped nanotubes junction case.

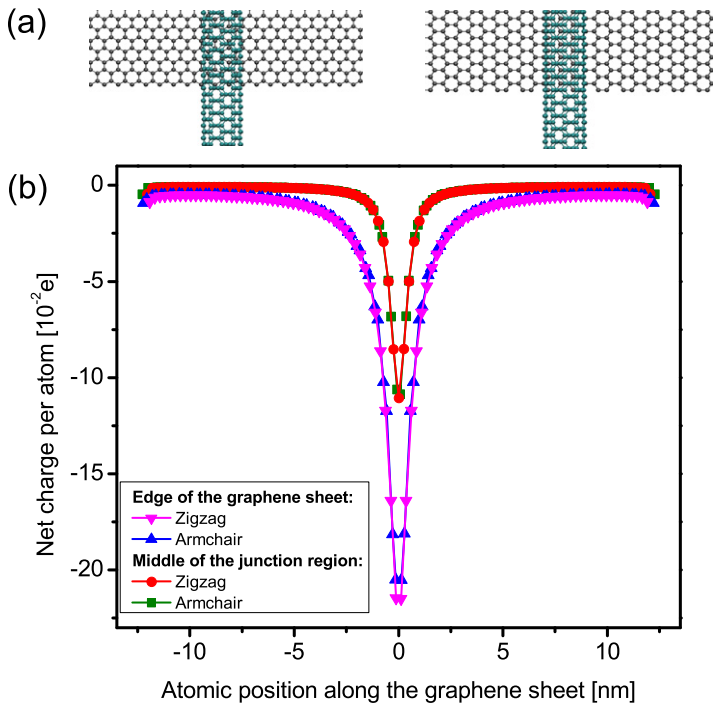

Figure 13. (a) Edge geometry: zigzag (left), armchair (right). (b) Net charge per atom in the junction region along the width of the graphene flake for different edge configurations.

3.2.6. Effects of the edges of the graphene flake. Until now, we have been focused on the part of the junction where the charge profile does not experience significant variation along the width of the graphene sheet. In this section we focus on the edge row of the graphene sheet that takes part into the junction (i.e. the row for $y = -l/2$). From the previous section, the net charge depletion for this particular row presents a different behavior and reaches higher values than for rows in the middle of the junction. Figure 11(d) shows that the maximal depletion value on the edge row is $\sim -20.5 \times 10^{-2}e$ when for the middle part of the junction, the maximal value is only around $\sim -10.8 \times 10^{-2}e$. For the edge row, besides the higher maximal value, the peak in the charge profile has a broaden shape, meaning that the influence of the CNT extends further in the graphene sheet ($l_{5\%\,\mathrm{max}} \sim 3.30$ nm).

So far, the junction region has been involved graphene sheet with armchair edges. Therefore, we performed calculations for junctions with zigzag edges as represented in figure 13(a). As illustrated in figure 13(b), for both edge configurations, the maximum of net charge depletion in the graphene flake is reached in the junction region for the closest atoms to the CNT. The difference of edge configuration has a substantial influence only on the net charge per atom in the graphene flake for the atomic row forming the edge itself. There, the atoms of the zigzag edges have a higher charge depletion value than their armchair counterpart. The maximum depletion is for zigzag edges about $-21.4 \times 10^{-2}e$ when it is about $-20.5 \times 10^{-2}e$ for armchair edges. For atoms located away from the edges, as expected, the influence of the edge configuration is less prevalent. The value for the maximal depletion for the zigzag configuration is $\sim -11.0 \times 10^{-2}e$ whereas for the armchair configuration it is $\sim -10.8 \times 10^{-2}e$.

If we consider $l_{5\%\,\max}$ as defined in section 3.2.4 for a cut along the graphene in a middle of the junction, there is no significant variation due to the type of edge involve in the junction ($l_{5\%\,\max} \sim 1.90$ nm). Only on the edge row $l_{5\%\,\max}$ does slightly differ depending on the edge characteristic($l_{5\%\,\max} \sim 3.40$ nm for zigzag edges, $l_{5\%\,\max} \sim 3.30$ nm for armchair edges).

The edge of the graphene sheet part of the junction shows a higher depletion effect than the atomic rows in the middle of the junction. Thus the length over which the CNT affects the charge distribution in the edge atomic row is larger than for the rest of the junction region. The nature of the edge geometry does not significantly affect the charge distribution along the edge row, only a slight increase in the charge depletion can be observed when using zigzag edges. This most likely reflects a limitation of a model purely based on electrostatic considerations.

3.2.7. Effects of the potential difference. In this part, the effects of the electrical potential difference on the charge profile are presented. In experimental works the electrical potential difference between the graphene and the CNT may vary, in particular if the graphene is back-gated as it is in common transport measurement technique. We demonstrate that the charge distribution scales proportionally with the potential difference $\Delta V = V_{\rm cnt} - V_{\rm gra}$. The shape of the charge profile in the graphene sheet as well as the length over which the CNT affects the charge in the graphene do not change with the potential difference.

We have used the same geometry as in section 3.2.5 for an uncapped CNT (5,5). Through all the previous calculations, the potential difference has been kept at $\Delta V = V_{\rm cnt} - V_{\rm gra} = 9$ V with $V_{\rm gra} = 1$ V and $V_{\rm cnt} = 10$ V. The graphene sheet has been hold at the same potential through all calculations ($V_{\rm gra} = 1$ V), while letting the potential difference taking three different values: $\Delta V = 5$, 15 and 18 V. The results of these calculations as well as the one obtained previously with $\Delta V = 9$ V have been plotted in figure 14. The charge profile on the graphene sheet for different ΔV exhibits the same behavior as in the previous sections. Thus the maximum depletion is found for atoms close to the CNT and the profile presents a sharp decrease of the depletion a few atomic rows away.

As depicted in the inset in the right part of figure 14, the values for the maximal depletion ranges from $-6.0 \times 10^{-2} e$ for $\Delta V = V_{\rm cnt} - V_{\rm gra} = 5$ V to $-22.9 \times 10^{-2} e$ for $\Delta V = 18$ V and presents a linear behavior with respect to ΔV. For the mean value of the net charge in the graphene sheet, the same observations can be seen. Thus the charge profile seems to scale proportionally with the potential difference ΔV. This is a direct consequence of the charge–dipole model from which the right-hand side of the system of linear equations are proportional to ΔV. This trend is confirmed if we normalize the charge profiles obtained for the considered ΔV to the actual potential difference ΔV. We obtain then the unique profile depicted in the right part of figure 14.

4. Discussion

In this section, we compare the results from our analytic calculations to the charge–dipole model. We first determine how the influence length $l_{5\%\,\max}$ scales with the radius of the CNT for both models. Then we study how the distance between the two sp^2 carbon allotropes does affect the charge distributions in the graphene.

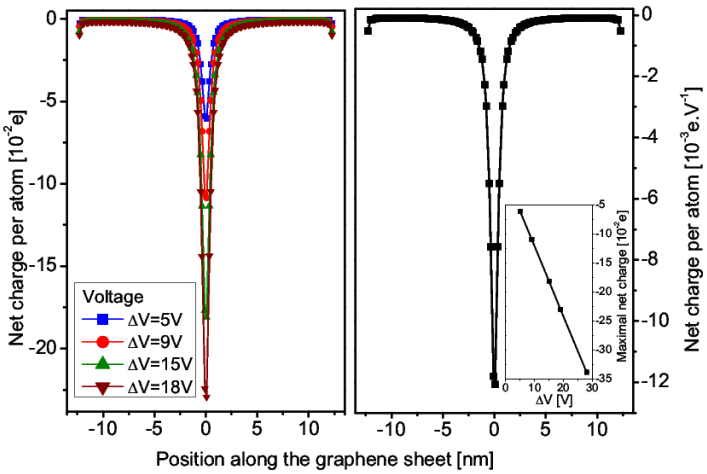

Figure 14. (left) Net charge profile along the length of the graphene sheet in the middle of the junction region for $\Delta V = 5$, 9, 15 and 18 V. (right) Net charge profile along the length of the graphene sheet in the middle of the junction region normalized to the potential difference ΔV. Inset: maximum charge depletion for several potential differences ΔV.

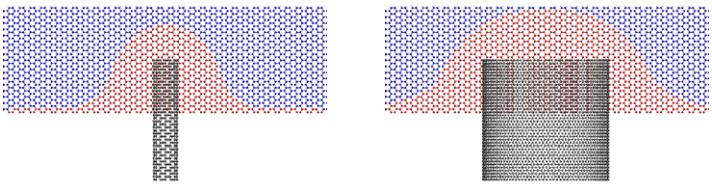

Figure 15. View of the extension of the CNT influence on the graphene sheet for a CNT (7,7) (left) and a CNT (37,37) (right). Atoms in red have a net charge $|q| \geqslant |q|_{5\%\,\max}$, while atoms in blue have a net charge $|q| \leqslant |q|_{5\%\,\max}$.

4.1. Scaling of the influence length $l_{5\%\,\max}$ with the radius of the CNT

Here we investigate the scaling of the influence length $l_{5\%\,\max}$ with the radius by replacing the CNT (5,5) used for the previous computations by tubes with a higher radius. We have used 12 different armchair CNT (n, n) with radii ranging from $\sim$0.5 to $\sim$3.35 nm (and the chiral index n ranging from 7 to 50), giving then 12 different junction configurations. The equilibrium distance between the tubes and the graphene has been inferred from the results of section 2. For each junction configuration, the influence length $l_{5\%\,\max}$ is determined. In order to be able to study how the influence region on the graphene sheet changes with the radius of the CNT, $l_{5\%\,\max}$ has been normalized to the radius of the CNT.

As clearly seen from the two charge distributions in figure 15, the influence of the CNT on the graphene sheet tends to be more restricted to regions close to the CNT when the radius increases. This trend is clearly to be seen in the variation of $l_{5\%\,\max}$ with the radius of the CNT for either analytic calculations or charge–dipole model (figure 16). The charge–dipole model gives for the CNT (50,50) a influence length $l_{5\%\,\max}$ of only about 1.7 times the radius of the tube itself, while for the tube (7,7) $l_{5\%\,\max}$ is about 4.5 times the radius. The results of the analytic calculations yield higher values for $l_{5\%\,\max}$ but follows the same tendency as the charge–dipole model, $l_{5\%\,\max} = 1.9$ for the CNT (50,50) and $l_{5\%\,\max} = 5.6$ for CNT (7,7).

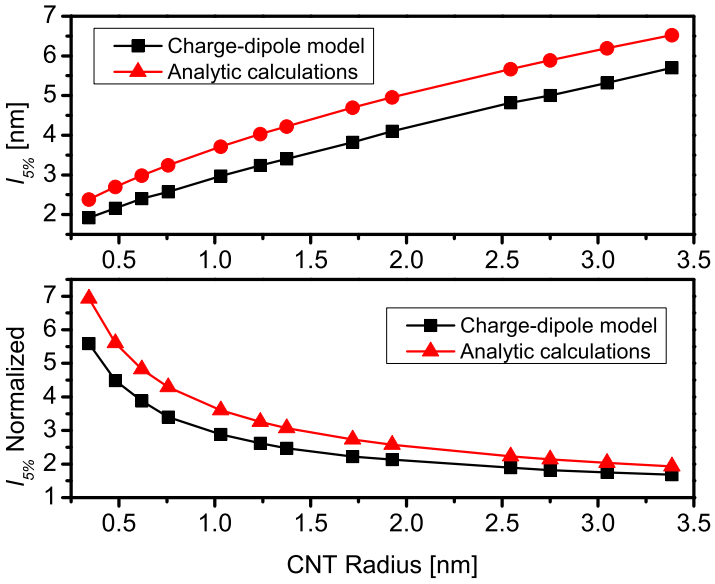

Figure 16. Influence length $l_{5\%\,\mathrm{max}}$ versus the radius of the CNT used for the junction (top). $l_{5\%\,\mathrm{max}}$ has been normalized to the radius of the CNT (bottom). $l_{5\%\,\mathrm{max}}$ has been analytically computed and using the charge–dipole model.

A important point in the analytic calculations is the lack of edge effects, since the graphene and the CNT are modeled by the cross-section of an infinite graphene sheet and the cross-section of an infinite cylinder. The values for $l_{5\%\,\mathrm{max}}$ are taken far from the edges in the case of the charge–dipole model. Thus edge effects can be ruled out to justify the differences arising between the two models. A reliable explanation for the different $l_{5\%\,\mathrm{max}}$ values between the two models lies in the dipole–charge interaction that tends to prevent the charge from spreading out in the graphene sheet and pin them to the junction region. Additionally, as the diameter of the tube is increasing the two models tend to the same normalized values. It is already clear that the distance between that CNT and the graphene sheet is significant role in the electrostatic landscape of the junction.

4.2. Effects of the carbone nanotube–graphene distance

Now we discuss the effect of the CNT–graphene distance $d_{\mathrm{CNT-Gra}}$ on the charge distribution in the graphene sheet. In section 2, the distance between a CNT (5,5) and a graphene sheet has been computed. To our knowledge, no experimental values are available for the equilibrium distance between a CNT and a graphene sheet. Furthermore, the equilibrium distance may vary with the experimental conditions. In particular for graphene-like field-effect devices and given the π–π nature of the CNT–graphene interactions, the gate voltage sweep may draw the tube toward the graphene or pull it away.

We have carried the calculations for distances within a large range that covers values around the equilibrium distance for a (5,5) CNT. Here we have chosen a range from $d_{\mathrm{CNT-Gra}} =$ 2.4–3.8 Å.[4]

[4] It is important to note that the reduction of the CNT–graphene distance is highly limited due to the strong short range repulsive forces.

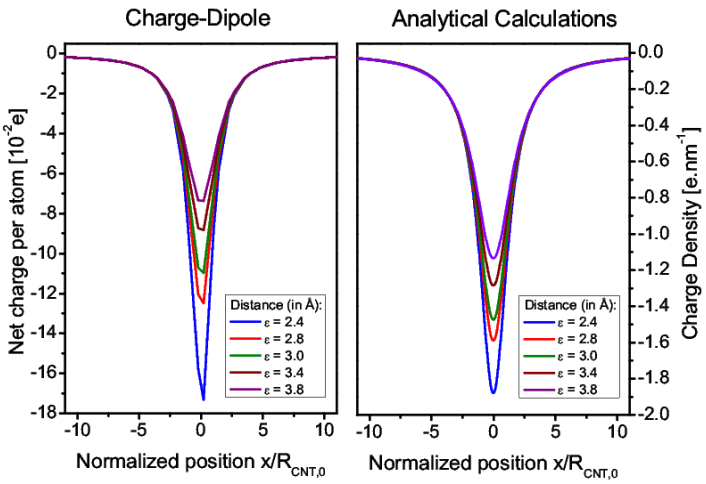

Figure 17. (left) Net charge profile in the graphene given by the charge–dipole model for different equilibrium distances $d_{\mathrm{CNT-Gra}}$. (right) Charge density profile calculated analytically in the graphene for different equilibrium distances $d_{\mathrm{CNT-Gra}}$.

The charge distribution profile across the graphene sheet is represented in figure 17 for several $d_{\mathrm{CNT-Gra}}$ and for both models. The overall shape of the profile does not change significantly with the distance $d_{\mathrm{CNT-Gra}}$. Indeed, the region of influence of the CNT is still restrained to a few atomic rows around the CNT and does not extend far in the graphene sheet. The only noticeable modification is the value of the charge distribution peak. The closer the tube is to the graphene sheet, the higher the value of the maximum of charge. Thus, the variation of $d_{\mathrm{CNT-Gra}}$ does only affect significantly the atoms located in the vicinity of the CNT.

Since both models give the same trend, we use the charge–dipole model to study in more detail the charge variation with the distance $d_{\mathrm{CNT-Gra}}$ in the first rows of atoms close to the CNT. The closest atom to the CNT (labeled as Max figure 18) undergoes the most dramatic change in net charge, carrying for $d_{\mathrm{CNT-Gra}} = 2.4$ Å a net charge of $-17.3 \times 10^{-2}e$ and for $d_{\mathrm{CNT-Gra}} = 3.8$ Å a net charge of $-7.4 \times 10^{-2}e$. This behavior is clearly to be seen in figure 18, where the net charge has been represented for atoms sitting at several distances from the closest one to the CNT. The net charge has been normalized for each atomic row to the one for the distance $d_{\mathrm{CNT-Gra}} = 2.4$ Å. For the atoms sitting from one row to three rows away from the closest atom to the CNT, the change in the net charge is significant when the distance $d_{\mathrm{CNT-Gra}}$ varies. When compared to the net charge these atoms carry for $d_{\mathrm{CNT-Gra}} = 2.4$ Å, the net charge loss is about 0.6 times for the first row atom and for the third row atoms about 0.15 times. For rows further away, the loss is smaller and it becomes eventually negligible for the atom five rows away from the closest one to the CNT, meaning that the change in the distance $d_{\mathrm{CNT-Gra}}$ has no more impact on the net charge. We note that our findings are in good agreement with the studies of metal–graphene junctions [9–11] as well as metal–dielectric–graphene junctions [117, 118] which report that the distance between a physically adsorbed metal and a graphene sheet is crucial to locate the Fermi level below the metal contact.

The charge distribution around the junction is therefore strongly governed by the distance between the CNT and the graphene sheet. While a larger size of the CNT would enlarge the zone of influence of the CNT on the graphene sheet, the increase of the equilibrium distance counterbalances it up to the point of becoming dominant.

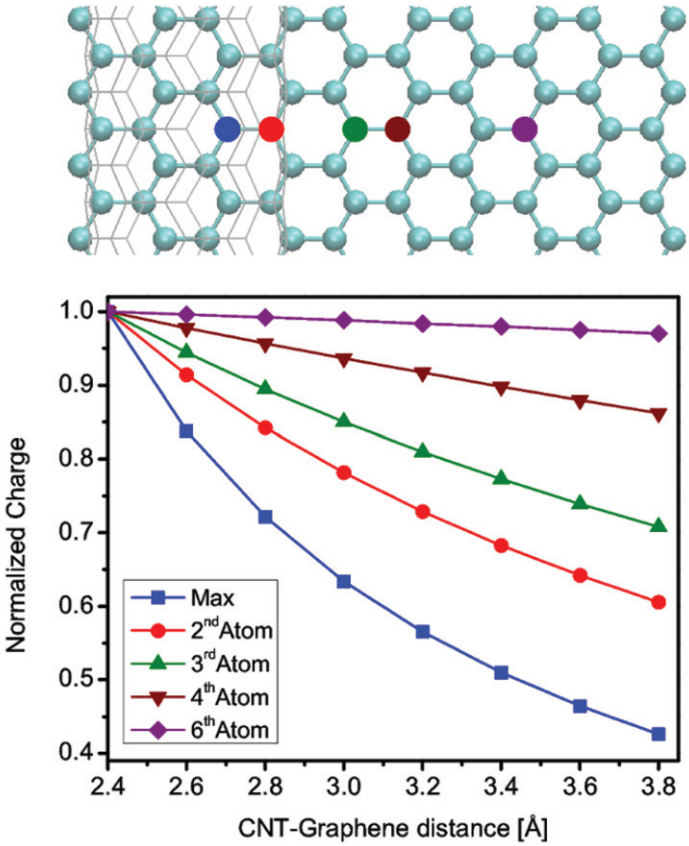

Figure 18. Normalized charge versus the CNT–graphene distance for the atom closest to the CNT (Max), the second closest, the third closest, the fourth closest and sixth closest. A sketch of the junction's geometry with the corresponding atoms is shown above.

5. Conclusions

To summarize this work, we have studied the electrostatic behavior of a CNT–graphene junction. We first calculated the equilibrium distance between the CNT and graphene sheet and found that the larger the diameter the further apart the two sp^2 carbon structures up to the two dimensional limit of two AB stacked graphene layers are. The CNT–graphene distance constitutes an important parameter for the description of the geometry used for the calculations. On one side, we performed electrostatic analytic calculations solving the Poisson's equation by conformal mapping techniques. On the other side, we have used a charge–dipole model.

For both models, we were able to describe the charge depletion/accumulation at a CNT–graphene junction. The influence of the CNT on the charge distribution in the graphene sheet has been analyzed by defining the length of influence of the CNT on the graphene sheet $l_{5\%\,\mathrm{max}}$. We showed that for small radius CNTs the influence extends in the graphene sheet over a length up to ∼6–7 times the radius while for large CNT radius the influence length was found to be ∼1.5–2 times the radius. Therefore, we could conclude that the influence of the CNT on charge distribution in the graphene sheet remains restrained to a region close to the junction region and does not extend deeper in the graphene sheet. We have also seen that a closed CNT accumulates fewer charges than the open-end ones. While the electrostatic does not seem to be

strongly sensitive to the edge quality, we have demonstrated that an increase of the potential difference between the CNT and the graphene sheet does not extend $l_{5\%\,\max}$. Since the distance between the CNT and the graphene sheet can strongly tune the charge distribution, it is rather likely that it will also affect the charge injection from the tube to the graphene. Finally, our work opens the way for the theoretical study of the electronic transport in CNT–graphene junctions.

Acknowledgments

We acknowledge I Beljakov, D Beljonne, S Bera, M Bürkle, R Du, A Durand, F Evers, H Hölscher, K Hönes, S Hong, M Huttin, I Kondov, R Korytár, V Meded, P Ostrovsky, D Sung, F Symalla, M van Setten, F Triozon, W Wenzel, F von Wrochem and F Wu for fruitful discussions. The use of the Steinbuch Centre for Computing (SCC) facility is gratefully acknowledged. RD's Shared Research Group SRG 1-33 received financial support by the Karlsruhe Institute of Technology within the framework of the German Excellence Initiative. This work was supported by the EU project MMM@HPC FP7-261594.

Appendix A. Extrapolation to determine the equilibrium distance for large CNT

For further applications (see section 4.1), we need to determine the equilibrium distance for large radii CNT (n,n) with chiral index up to $n = 50$ by extrapolation of our calculations for smaller CNT. The data obtained with MOPAC for the tubes CNT (5,5), (9,9) and (15,15) have been used to determine the following function:

$$d_{\mathrm{eq}} = d_0 + A\ \exp\left(-\frac{R}{R_0}\right) \tag{A.1}$$

with d_{eq} the equilibrium distance for a CNT with a radius of R, A and R_0 are free parameters determined by the extrapolation (here $A = -0.34$ Å and $R_0 = 103$ Å). The limit for the equilibrium distance has been set to be the graphene interlayer distance (i.e. $d_0 = 3.34$ Å). The equilibrium distance for a CNT (50,50) which has a radius of $\sim$34 Å is about 3.16 Å. Thus, for over an order magnitude change for the radius, the equilibrium distance increases from about 0.14 Å (figure A.1).

Appendix B. Conformal mapping transformations

We detail the two conformal mapping transformations used in section 3.1. The initial geometry is described in the $(O_{x,y}, x, y)$ coordinate system. The first map transforms this coordinates system into $(O_{u,v}, u, v)$. In the final coordinates system $(O_{p,q}, p, q)$, the solution of the Laplace's equation is straightforward. The first conformal mapping transformation used $G(z)$ is given by

$$G(z) = w = \frac{(R_{\mathrm{cnt},0} - \epsilon)\epsilon}{2R_{\mathrm{cnt},0} - \epsilon} + \frac{\boldsymbol{i}\epsilon^2}{z - 2\boldsymbol{i}\epsilon}, \tag{B.1}$$

where $z = x + \boldsymbol{i}\,y$ and $w = u + \boldsymbol{i}\,v$, $z, w \in \mathbb{C}$ and $x, y, u, v \in \mathbb{R}$. By applying $G(z)$ to the initial geometry (figure 4(a))) we obtained the geometry shown in figure 4(b)). Thus, the original

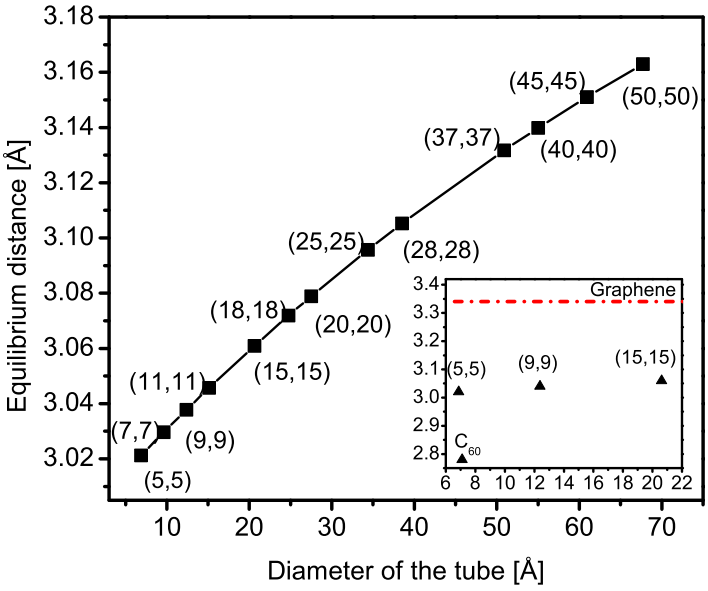

Figure A.1. Extrapolation procedure to extract the equilibrium distance for large CNT (n,n) with $n \leqslant 50$ determined by using equation (A.1).

circle $C_{\mathrm{cnt},0}$ (radius: $R_{\mathrm{cnt},0}$ center: $O_{x,y}$) is mapped into a new circle $C_{\mathrm{cnt},1}$ (radius: $R_{\mathrm{cnt},1}$, center: $O_{u,v}$) while the straight line is transformed into a circle $C_{\mathrm{gra},1}$ (radius: $R_{\mathrm{gra},1}$, center: $A_{u,v}$). The coordinates of the point $A_{u,v}$ are given by

$$u_{A_{u,v}} = \frac{\left(2R_{\mathrm{cnt},0} - 3\epsilon\right)\epsilon}{4\left(2R_{\mathrm{cnt},0} - \epsilon\right)}, \qquad v_{A_{u,v}} = 0. \tag{B.2}$$

The expression for the radii are given by

$$R_{\mathrm{cnt},1} = \frac{R_{\mathrm{cnt},0}\epsilon}{|\epsilon - 2R_{\mathrm{cnt},0}|}, \qquad R_{\mathrm{gra},1} = \epsilon/4. \tag{B.3}$$

For later use, we defined u_1 and u_2 as

$$u_1 = u_{A_{u,v}} - R_{\mathrm{gra},1}, \qquad u_2 = u_{A_{u,v}} + R_{\mathrm{gra},1}. \tag{B.4}$$

For the second conformal mapping transformation $H(w)$, we used a Moebius transformation in order to map the circles previously obtained by using $G(z)$ into two concentric circles centered on $O_{p,q}$. $H(w)$ is given by

$$H(w) = t = \frac{w - ab}{aw - b} \tag{B.5}$$

with $t = p + \boldsymbol{i}q$, $t \in \mathbb{C}$, $p, q \in \mathbb{R}$ and a and b defined by

$$a = \frac{R_{\mathrm{cnt},1}^2 + u_1 u_2 + \sqrt{(R_{\mathrm{cnt},1}^2 - u_1^2)(R_{\mathrm{cnt},1}^2 - u_2^2)}}{R_{\mathrm{cnt},1}(u_1^2 + u_2^2)} \tag{B.6}$$

$$b = R_{\mathrm{cnt},1}. \tag{B.7}$$

Thus by applying the transformation $H(w)$, the circle $C_{\mathrm{cnt},1}$ is mapped into the circle $C_{\mathrm{cnt},2}$ (radius: $R_{\mathrm{cnt},2}$) and the circle $C_{\mathrm{gra},1}$ is transformed into the circle $C_{\mathrm{gra},2}$ (radius: $R_{\mathrm{gra},2}$). Both circles $C_{\mathrm{cnt},2}$ and $C_{\mathrm{gra},2}$ are centered at $O_{\mathrm{p,q}}$ as shown in figure 4(c).

$R_{\mathrm{cnt},2}$ has a simple value since

$$R_{\mathrm{cnt},2} = 1, \tag{B.8}$$

while $R_{\mathrm{gra},2}$ is given by

$$R_{\mathrm{gra},2} = \frac{R_{\mathrm{cnt},1}^2 - u_1 u_2 + \sqrt{(R_{\mathrm{cnt},1}^2 - u_1^2)(R_{\mathrm{cnt},1}^2 - u_2^2)}}{R_{\mathrm{cnt},1}(u_1^2 - u_2^2)}. \tag{B.9}$$

By using the transformation G and H, the expression of $p(x, y)$ and $q(x, y)$ can be inferred since

$$\begin{cases} \Re(G(z)) = \Re(w) = u(x, y), \\ \Im(G(z)) = \Im(w) = v(x, y) \end{cases}$$

and

$$\begin{cases} \Re(H(w)) = \Re(t) = p(u, v), \\ \Im(H(w)) = \Im(t) = q(u, v), \end{cases}$$

where $\Re$ stands for the real part and $\Im$ for the imaginary part.

Appendix C. Charge–dipole model interaction terms

We sum up the charge–dipole interaction terms as presented in [102, 107]. Equation (4) in section 3.2.1 gives the expression of the total electrostatic energy. The charge–charge interaction term is given by

$$\frac{1}{2}\sum_{i,j} q_i T_{q-q}^{i,j} q_j, \tag{C.1}$$

where $T_{q-q}^{i,j}$ stands for the charge–charge interaction tensor in vacuum. If $r_{i,j}$ is the distance between the atom i and the atom j, and $\mathbf{r}_i$ the coordinate of the atom i, the regular expression for $T_{q-q}^{i,j}$ is then

$$T_{q-q}^{i,j} = \frac{1}{4\pi\epsilon_0}\frac{1}{r_{i,j}}. \tag{C.2}$$

The charge–dipole interaction term is

$$-\sum_{i,j} q_i \mathbf{T}_{q-p}^{i,j} \mathbf{p}_j, \tag{C.3}$$

where $T_{q-p}^{i,j}$ is the charge–dipole interaction tensor in the vacuum. The regular expression for $\mathbf{T}_{q-p}^{i,j}$ is

$$\mathbf{T}_{q-p}^{i,j} = -\nabla_{\mathbf{r}_i} T_{q-q}^{i,j}. \tag{C.4}$$

The dipole–dipole interaction term is

$$-\frac{1}{2}\sum_{i,j}\mathbf{p}_i \boldsymbol{T}^{i,j}_{p-p}\mathbf{p}_j, \tag{C.5}$$

where $T^{i,j}_{p-p}$ is the dipole–dipole interaction tensor in the vacuum. The regular expression for $\mathbf{T}^{i,j}_{p-p}$ is

$$\mathbf{T}^{i,j}_{p-p} = -\nabla_{\mathbf{r}_j}\otimes\nabla_{\mathbf{r}_i}\, T^{i,j}_{q-q}. \tag{C.6}$$

Using the equation (5) in the expressions for the interaction tensors terms leads then to the following expressions:

$$T^{i,j}_{q-q} = \frac{1}{4\pi\epsilon_0}\frac{\mathrm{erf}\left(\frac{r_{i,j}}{\sqrt{2}R}\right)}{r_{i,j}}, \tag{C.7}$$

$$\mathbf{T}^{i,j}_{q-p} = \frac{1}{4\pi\epsilon_0}\frac{\mathbf{r}_{i,j}}{r^3_{i,j}}\left[\mathrm{erf}\left(\frac{r_{i,j}}{\sqrt{2}R}\right) - \sqrt{\frac{2}{\pi}}\frac{r_{i,j}}{R}\exp\left(-r^2_{i,j}/2R^2\right)\right], \tag{C.8}$$

$$\begin{aligned}\mathbf{T}^{i,j}_{p-p} = \frac{1}{4\pi\epsilon_0}\frac{3\mathbf{r}_{i,j}\otimes\mathbf{r}_{i,j} - r^2_{i,j}\mathbf{Id}_3}{r^5_{i,j}} \times \Bigg\{&\left[\mathrm{erf}\left(\frac{r_{i,j}}{\sqrt{2}R}\right) - \sqrt{\frac{2}{\pi}}\frac{r_{i,j}}{R}\exp\left(-r^2_{i,j}/2R^2\right)\right]\\ &-\sqrt{\frac{2}{\pi}}\frac{1}{R^3}\frac{\mathbf{r}_{i,j}\otimes\mathbf{r}_{i,j}}{r^2_{i,j}}\exp\left(-r^2_{i,j}/2R^2\right)\Bigg\},\end{aligned} \tag{C.9}$$

where $\mathbf{Id}_3$ is the size 3 identity matrix and erf is the Gauss error function given by

$$\mathrm{erf}(x) = \frac{2}{\sqrt{\pi}}\int_0^x \exp(-t^2)\mathrm{d}t. \tag{C.10}$$

The limit case $r_{i,j}\to 0$ in expression (C.7), (C.8) and (C.10) gives for the self-energy terms

$$T^{i,i}_{q-q} = \frac{1}{4\pi\epsilon_0}\frac{\sqrt{2}}{\sqrt{\pi}R}, \tag{C.11}$$

$$\mathbf{T}^{i,i}_{p-q} = 0, \tag{C.12}$$

$$\mathbf{T}^{i,i}_{p-p} = -\frac{1}{4\pi\epsilon_0}\frac{\sqrt{2}}{3\sqrt{\pi}R^3}\mathbf{Id}_3. \tag{C.13}$$

In [103, 107], the dipole–dipole self-interaction $\mathbf{T}^{i,i}_{p-p}$ term is equal to $\alpha^{-1}_{\mathrm{iso}}$ which represent the polarizability of the carbon atoms in sp^2 carbon structures. Thus assuming an isotropic polarizability, the following relation can be used to link the parameter R (i.e. the width of the Gaussian distribution) and the polarizability using the following expression:

$$\frac{\alpha_{\mathrm{iso}}}{4\pi\epsilon_0} = 3\sqrt{\frac{\pi}{2}}R^3. \tag{C.14}$$

The parameter R has been then determined using experimental data to reproduce the mean polarizability of fullerenes and lateral polarizability of CNT [102].

The implementation of the charge–dipole model has been done using the C++ programming language. The resolution of the linear equation system was performed with the routine DGESV called by the C++ code. This routine is part of the LAPACK package [119] written in Fortran. Structures with up to about 10 000 atoms could be solved using the random access memory resources of the Opus Cluster from the Steinbuch Centre for Computing (SCC). The size of the systems handled with the charge–dipole model is therefore larger than with *ab initio* methods or even semi-empirical methods.

References

[1] Geim A K and Novoselov K S 2007 *Nature Mater.* **6** 183
[2] Pasanen P, Voutilainen M, Helle M, Song X and Hakonen P J 2012 *Phys. Scr.* **T146** 014025
[3] Novoselov K S, Falko V I, Colombo L, Gellert P R, Schwab M G and Kim K 2012 *Nature* **490** 192
[4] Castro Neto A H, Guinea F, Peres N M R, Novoselov K S and Geim A K 2009 *Rev. Mod. Phys.* **81** 109
[5] Das Sarma S, Adam S, Hwang E H and Rossi E 2009 *Rev. Mod. Phys.* **83** 407
[6] Schwierz F 2010 *Nature Nanotechnol.* **5** 487
[7] Xia F, Pereibenos V, Lin Y M, Wu Y and Avouris P 2011 *Nature Nanotechnol.* **6** 179
[8] Léonard F and Talin A A 2011 *Nature Nanotechnol.* **6** 773
[9] Giovannetti G, Khomyakov P A, Brocks G, Karpan V M, van den Brink J and Kelly P J 2008 *Phys. Rev. Lett.* **101** 026803
[10] Khomyakov P A, Giovannetti G, Rusu P C, Brocks G, van den Brink J and Kelly P J 2009 *Phys. Rev.* B **79** 195425
[11] Khomyakov P A, Starikov A A, Brocks G and Kelly P J 2010 *Phys. Rev.* B **82** 115437
[12] Barraza-Lopez S, Kindermann M and Chou M Y 2012 *Nano Lett.* **12** 3424
[13] Huard B, Stander N, Sulpizio J A and Goldhaber-Gordon D 2008 *Phys. Rev.* B **78** 121402
[14] Lee E J H, Balasubramanian K, Weitz R T, Burghard M and Kern K 2008 *Nature Nanotechnol.* **3** 486
[15] Golizadeh-Mojarad R and Datta S 2009 *Phys. Rev.* B **79** 085410
[16] Cayssol J, Huard B and Goldhaber-Gordon D 2009 *Phys. Rev.* B **79** 075428
[17] Nam Do V and Anh Le H 2012 *Appl. Phys. Lett.* **101** 161605
[18] Mohr M, Papagelis K, Maultzsch J and Thomsen C 2009 *Phys. Rev.* B **80** 205410
[19] Pellegrino F M D, Angilella G G N and Pucci R 2010 *Phys. Rev.* B **81** 035411
[20] Choi S-M, Jhi S-H and Son Y-W 2010 *Phys. Rev.* B **81** 081407
[21] Bera S, Arnold A, Evers F, Narayanan R and Wölfle P 2010 *Phys. Rev.* B **82** 195445
[22] Gerhard L, Moyen E, Balashov T, Ozerov I, Portail M, Sahaf H, Masson L, Wulfhekel W and Hanbücken M 2012 *Appl. Phys. Lett.* **100** 153106
[23] Gong W, Zhang W, Ren C, Ke X, Wang S, Huai P, Zhang W and Zhu Z 2013 *Appl. Phys. Lett.* **103** 143107
[24] Chen Z and Appenzeller J 2009 *Proc. Symp. VLSI Technol.* 128
[25] Blake P, Yang R, Morozov S V, Schedin F, Ponomarenko L A, Zhukov A A, Nair R R, Grigorieva I V, Novoselov K S and Geim A K 2009 *Solid State Commun.* **49** 1068
[26] Nagashio K, Nishimura T, Kita K and Toriumi A 2010 *Japan. J. Appl. Phys.* **49** 051304
[27] Russo S, Craciun M F, Yamamoto M, Morpurgo A F and Tarucha S 2010 *Physica* E **42** 677
[28] Venugopal A, Colombo L and Vogel E M 2010 *Appl. Phys. Lett.* **96** 013512
[29] Nagashio K, Nishimura T, Kita K and Toriumi A 2010 *Appl. Phys. Lett.* **97** 143514
[30] Matsuda Y, Deng W-Q and Goddard W A 2010 *J. Phys. Chem.* C **114** 17845
[31] Malec C and Davidovic' D 2011 *Phys. Rev.* B **84** 033407
[32] Huang B-C, Zhang M, Wang Y and Woo J 2011 *Appl. Phys. Lett.* **99** 032107

[33] Franklin A D, Han S-J, Bol A A and Haensch W 2011 *IEEE Electron. Device Lett.* **32** 1035
[34] Franklin A D, Han S-J, Bol A A and Perebeinos V 2012 *IEEE Electron. Device Lett.* **33** 17
[35] Watanabe E, Conwill A, Tsuya D and Koide Y 2012 *Diamond Relat. Mater.* **24** 171
[36] Knoch J, Chen Z and Appenzeller J 2012 *IEEE Trans. Nanotechnol.* **11** 513
[37] Liu H, Kondo H and Ohno T 2012 *Phys. Rev.* B **86** 155434
[38] Moon J S *et al* 2012 *Appl. Phys. Lett.* **100** 203512
[39] Lin Y-F, Wang S-T, Pao C-C, Li Y-C, Lai C-C, Lin C-K, Hsu S-Y and Jian W-B 2013 *Appl. Phys. Lett.* **102** 033107
[40] Kane A A, Sheps T, Branigan E T, Apkarian V A, Cheng M H, Hemminger J C, Hunt S R and Collins P G 2009 *Nano Lett.* **9** 3586
[41] Hong T-K, Lee D W, Choi H J, Shin H S and Kim B-S 2010 *ACS Nano* **4** 3861
[42] Chai Y, Hazeghi A, Takei K, Chen H Y, Chan P C H, Javey A and and Wong H-S P 2010 *IEDM Technol. Dig.* 210
[43] Chai Y, Hazeghi A, Takei K, Chen H-Y, Chan P, Javey A and Wong H-S 2012 *IEEE Trans. Electron. Device* **59** 12
[44] Liu G, Rumyantsev S, Shur M and Balandin A A 2012 *Appl. Phys. Lett.* **100** 033103
[45] Tamaoki M, Kishimoto S, Ohno Y and Mizutani T 2012 *Appl. Phys. Lett.* **101** 033101
[46] Tamaoki M, Kishimoto S and Mizutani T 2013 *Appl. Phys. Lett.* **103** 033120
[47] Jiao L, Zhang L, Ding L, Liu J and Dai H 2010 *Nano Res.* **3** 387
[48] Ouyang F, Xiao J, Guo R, Zhang H and Xu H 2009 *Nanotechnology* **20** 055202
[49] Ouyang Y and Guo J 2010 *Appl. Phys. Lett.* **97** 263115
[50] Botello-Mendez A R, Cruz-Silva E, Romo-Herrera J M, Lopez-Urías F, Terrones M, Sumpter B G, Terrones H, Charlier J-C and Meunier V 2011 *Nano Lett.* **11** 3058
[51] Masum Habib K M and Lake R K 2012 *Phys. Rev.* B **86** 045418
[52] Li B *et al* 2010 *Adv. Mater.* **22** 3058
[53] Jang S, Jang H, Lee Y, Suh D, Baik S, Hong B H and Ahn J-H 2010 *Nanotechnology* **21** 425201
[54] Standley B, Mendez A, Schmidgall E and Bockrath M 2012 *Nano Lett.* **12** 1165
[55] Lee S-K, Jang H Y, Jang S, Choi E, Hong B H, Lee J, Park S and Ahn J-H 2012 *Nano Lett.* **12** 3472
[56] Lee S, Lee K, Liu C-H, Kulkarni G S and Zhong Z 2012 *Nature Commun.* **3** 1018
[57] Ramuz M P, Vosgueritchian M, Wei P, Wang C, Gao Y, Wu Y, Chen Y and Bao Z 2012 *ACS Nano* **6** 10384
[58] Benz C, Thümer M, Wu F, Ben Aziza Z, Mohrmann J, Löhneysen H V, Watanabe K, Taniguchi T and Danneau R 2013 *Appl. Phys. Lett.* **102** 033505
[59] Chae S H *et al* 2013 *Nature Mater.* **12** 403
[60] Robert P T, Du R, Wu F, Hennrich F, Kappes M M, Löhneysen H v and Danneau R in preparation
[61] Su W S, Leung T C and Chan C T 2007 *Phys. Rev.* B **76** 235413
[62] Suzuki S, Bower C, Watanabe Y and Zhou O 2000 *Appl. Phys. Lett.* **76** 4007
[63] Yu Y-J, Zhao Y Y, Ryu S, Brus L E, Kim K S and Kim P 2009 *Nano Lett.* **9** 3430
[64] Wang W X, Liang S H, Yu T, Li D H, Li Y B and Han X F 2011 *J. Appl. Phys.* **109** 07C501
[65] Fuhrer M S *et al* 2000 *Science* **288** 494
[66] Gonzalez J, Guinea F and Herrero J 2009 *Phys. Rev.* B **79** 165434
[67] Novaes F D, Rurali R and Ordejon P 2010 *ACS Nano* **4** 7596
[68] Ma K L, Yan X H, Guo Y D and Xiao Y 2011 *Eur. Phys. J.* B **83** 487
[69] Lee J, Varshney V, Brown J S, Roy A K and Farmer B L 2012 *Appl. Phys. Lett.* **100** 183111
[70] Dimitrakakis G K, Tylianakis E and Froudakis G E 2008 *Nano Lett.* **8** 3166
[71] Lin J, Zhang C, Yan Z, Zhu Y, Peng Z, Hauge R H, Natelson D and Tour J M 2013 *Nano Lett.* **13** 72
[72] Janssen J W, Lemay S G, Kouwenhoven L P and Dekker C 2002 *Phys. Rev.* B **65** 115423
[73] Gao B, Komnik A, Egger R, Glattli D C and Bachtold A 2004 *Phys. Rev. Lett.* **92** 216804
[74] Gao B, Chen Y F, Fuhrer M S, Glattli D C and Bachtold A 2005 *Phys. Rev. Lett.* **95** 196802
[75] Cook B G, French W R and Varga K 2012 *Appl. Phys. Lett.* **101** 153501

[76] Paulson S, Helser A, Nardelli M B, Taylor I I R M, Falvo M, Superfine R and Washburn S 2000 *Science* **290** 1742
[77] Hunley D P, Johnson S L, Stieha J K, Sundararajan A, Meacham A T, Ivanov I N and Strachan D R 2011 *ACS Nano* **5** 6403
[78] Gan L, Liu S, Li D-N, Hang H, Cao Y, Shen Q, Wang Z X, Wang Q and Guo X-F 2010 *Acta Phys. Chim. Sin.* **26** 1151
[79] Pei T, Xu H, Zhang Z, Wang Z, Liu Y, Li Y, Wang S and Peng L-M 2011 *Appl. Phys. Lett.* **99** 113102
[80] Engels S, Weber P, Terrés B, Dauber J, Meyer C, Volk C, Trellenkamp S, Wichmann U and Stampfer C 2013 *Nanotechnology* **24** 035204
[81] Paulus G L C, Wang Q H, Ulissi Z W, McNicholas T P, Vijayaraghavan A, Shih C-J, Jin Z and Strano M S 2013 *Small* **9** 1954
[82] DiVincenzo D P, Mele E J and Holzwarth N A W 1983 *Phys. Rev.* B **27** 2458
[83] Charlier J-C and Michenaud J-P 1993 *Phys. Rev. Lett.* **70** 1858
[84] Kolmogorov A N and Crespi V H 2005 *Phys. Rev.* B **71** 235415
[85] Dappe Y J, Ortega J and Flores F 2009 *Phys. Rev.* B **79** 165409
[86] Seydou M, Marsaudon S, Buchoux J, Aimé J-P and Bonnot A-M 2009 *Phys. Rev.* B **80** 245421
[87] Seydou M, Dappe Y J, Marsaudon S, Aimé J-P, Bouju X and Bonnot A-M 2011 *Phys. Rev.* B **83** 045410
[88] Stewart J J P 2007 *J. Mol. Model.* **13** 1173
[89] Řezač J, Fanfrlík J, Salahub D and Hobza P 2009 *J. Chem. Theor. Comput.* **5** 1749
[90] Jurečka P, Černý J, Hobza P and Salahub D R 2007 *J. Comput. Chem.* **28** 555
[91] Lukas M, Meded V, Vijayaraghavan A, Song L, Ajayan P M, Fink K, Wenzel W and Krupke R 2013 *Nature Commun.* **4** 1319
[92] Dappe Y J, Basanta M A, Flores F and Ortega J 2006 *Phys. Rev.* B **74** 205434
[93] Švec M, Merino P, Dappe Y J, González C, Abad E, Jelínek P and Martín-Gago J A 2012 *Phys. Rev.* B **86** 121407
[94] Li Z-B and Wang W-L 2006 *Chin. Phys. Lett.* **23** 1616
[95] Silvestrov P G and Efetov K B 2008 *Phys. Rev.* B **77** 155436
[96] Schinzinger R and Laura P A A 2003 *Conformal Mapping: Methods and Applications (Books on Mathematics Series)* (New York: Dover)
[97] Rycerz A, Recher P and Wimmer M 2009 *Phys. Rev.* B **80** 125417
[98] Olson M L and Sundberg K R 1978 *J. Chem. Phys.* **69** 5400
[99] Applequist J, Carl J R and Fung K-K 1972 *J. Am. Chem. Soc.* **94** 2952
[100] Stern H A, Kaminski G A, Banks J L, Zhou R, Berne B J and Friesner R A 1999 *J. Phys. Chem.* B **103** 4730
[101] Shanker B and Applequist J 1994 *J. Phys. Chem.* **98** 6486
[102] Mayer A 2005 *Appl. Phys. Lett.* **86** 153110
[103] Mayer A 2005 *Phys. Rev.* B **71** 235333
[104] Wang Z and Devel M 2007 *Phys. Rev.* B **76** 195434
[105] Wang Z, Zdrojek M, Melin T and Devel M 2008 *Phys. Rev.* B **78** 085425
[106] Wang Z and Scharstein R W 2009 *Chem. Phys. Lett.* **489** 229
[107] Mayer A 2007 *Phys. Rev.* B **75** 045407
[108] Mayer A, Lambin P and Astrand P-O 2008 *Nanotechnology* **19** 025203
[109] Mayer A and Astrand P-O 2008 *J. Phys. Chem.* A **112** 1277
[110] Langlet R, Mayer A, Geuquet N, Amara H, Vandescuren M, Henrard L, Maksimenko S and Lambin P 2008 *Diamond Relat. Mater.* **16** 2145
[111] Peres N M R, Guinea F and Castro Neto A H 2006 *Phys. Rev.* B **73** 125411
[112] Fernandez-Rossier J M, Palacios J J and Brey L 2007 *Phys. Rev.* B **75** 205441
[113] Wang Z 2008 Propriétés électro-mécaniques des nanotubes de carbone *PhD Thesis* Université de Franche-Comté
[114] Keblinski P, Nayak S K, Zapol P and Ajayan P M 2002 *Phys. Rev. Lett.* **89** 255503

[115] Li C and Chou T-W 2006 *Appl. Phys. Lett.* **89** 063103
[116] Saito R, Dresselhaus G and Dresselhaus M S 1998 *Physical Properties of Carbon Nanotubes* (London: Imperial College)
[117] Bokdam M, Khomyakov P A, Brocks G, Zhong Z and Kelly P J 2011 *Nano Lett.* **11** 4631
[118] Bokdam M, Khomyakov P A, Brocks G and Kelly P J 2013 *Phys. Rev.* B **87** 075414
[119] Anderson E *et al* 1999 *LAPACK Users' Guide* 3rd edn (Philadelphia, PA: Society for Industrial and Applied Mathematics)